

Carderock Division, Naval Surface Warfare Center

9500 MacArthur Blvd.
West Bethesda, Maryland 20817-5700

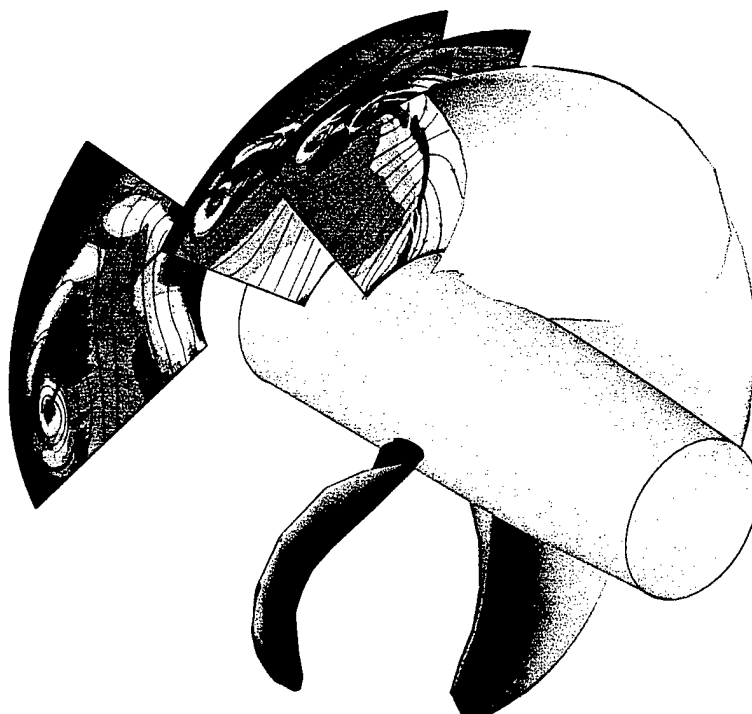
CRDKNSWC/HD-1460-02 May 1998

Hydromechanics Directorate
Research and Development Report

Cavitation and 3-D LDV Tip-Flowfield Measurements of Propeller 5168

by

Christopher J. Chesnakas
and
Stuart D. Jessup



19980623 107



Approved for public release. Distribution Unlimited.

CRDKNSWC/HD-1460-02 Cavitation and 3-D LDV Tip-Flowfield Measurements of Propeller 5168



DEPARTMENT OF THE NAVY
NAVAL SURFACE WARFARE CENTER
CARDEROCK DIVISION

CARDEROCK DIVISION HEADQUARTERS
DAVID TAYLOR MODEL BASIN
9500 MACARTHUR BOULEVARD
WEST BETHESDA, MD 20817-5700

IN REPLY REFER TO:

5605
5400:DMI
16 Jun 98

From: Commander, Carderock Division, Naval Surface Warfare Center
To: Chief of Naval Research, Office of Naval Research (ONR 333)

Subj: FORWARDING OF A REPORT

Encl: (1) Carderock Division, Naval Surface Warfare Center,
Hydromechanics Directorate Report, CRDKNSWC/HD-1460-02,
"Cavitation and 3-D LDV Tip-Flowfield Measurements of
Propeller 5168 by Christopher J. Chesnakas and
Stuart Jessup (May 1998)
(2) Customer Project Survey Form 5200-20A (Rev 4)

1. Enclosure (1) is forwarded for your information and retention.

2. It is requested that enclosure (2) be completed and returned to the Carderock Division, Naval Surface Warfare Center. Customer project surveys are conducted at the completion of a project. They are used at the Department level to control and verify the system process capability. The forms will be reviewed for customer comments, including complaints and recommendations. Corrective actions will be taken.

3. If you have any questions, please contact Dr. Frank B. Peterson, Code 5400, telephone number (301) 227-1418.

FRANK B. PETERSON
By direction

Subj: FORWARDING OF A REPORT

Copy to: (w/o encl (2))

ONR 334 (Rood)

NAVSEA 03Z5 (Crockett, Berberich)

NAVSEA 03DC (Crowe)

ARL/PSU (Knight, Billet, Brockett, Pauley, Zierke)

MIT (Kerwin)

EB (Cox)

MSU (Taylor, Whitfield)

Univ of Iowa (Stern)

AME (Scherer)

SAIC (Korpus)

Univ of Texas (Kinnas)

Univ of Tennessee (Merkle)

Univ of New Orleans (Vorus, Brown)

DTIC (2)

REPORT DOCUMENTATION PAGE			Form Approved OMB No. 0704-0188	
<small>Public reporting burden for this collection of information is estimated to average 1 hour per response, including the time for reviewing instructions, searching existing data sources, gathering and maintaining the data needed, and completing and reviewing the collection of information. Send comments regarding this burden estimate or any other aspect of this collection of information, including suggestions for reducing this burden, to Washington Headquarters Services, Directorate for Information Operations and Reports, 1215 Jefferson Davis Highway, Suite 1204, Arlington, VA 22202-4302, and to the Office of Management and Budget, Paperwork Reduction Project (0704-0188), Washington, DC 20503.</small>				
1. AGENCY USE ONLY (Leave blank)		2. REPORT DATE May 1998		3. REPORT TYPE AND DATES COVERED Research and Development, Mar 96 to Sep 97
4. TITLE AND SUBTITLE Cavitation and 3-D LDV Tip-Flowfield Measurements of Propeller 5168			5. FUNDING NUMBERS N0014-97WX-20181/AE	
6. AUTHOR(S) Christopher J. Chesnakas and Stuart D. Jessup				
7. PERFORMING ORGANIZATION NAME(S) AND ADDRESS(ES) Hydromechanics Directorate, Code 5400 Carderock Division, Naval Surface Warfare Center 9500 MacArthur Boulevard West Bethesda, MD 20817-5700			8. PERFORMING ORGANIZATION REPORT NUMBER CRDKNSWC/HD-1460-02	
9. SPONSORING / MONITORING AGENCY NAME(S) AND ADDRESS(ES) Ship Systems and Programs Directorate Carderock Division Naval Surface Warfare Center Bethesda, MD 20084-5000			10. SPONSORING / MONITORING AGENCY REPORT NUMBER	
11. SUPPLEMENTARY NOTES				
12a. DISTRIBUTION / AVAILABILITY STATEMENT Approved for public release. Distribution unlimited.			12b. DISTRIBUTION CODE	
13. ABSTRACT (Maximum 200 words) <p>Detailed velocity measurements were made of the velocity field behind Propeller 5168 in the Carderock Division, Naval Surface Warfare Center (CDNSWC) 36-inch water tunnel. The measurements were made in order to examine the behavior of the tip-vortex flow. A first set of measurements was made with a three-component Laser Doppler Velocimeter (LDV) system at four different advance coefficients and at four downstream stations. A second set of measurements was made with a three-component, coincident LDV system at a single advance coefficient and downstream station. The coincident set of measurements was of higher accuracy and included data on the Reynolds shear-stress terms. Plots are presented of the detailed tip-vortex structure, and the variation of this structure with advance coefficient and location is examined. Data on the thrust, torque, and cavitation performance of the propeller are also included.</p>				
14. SUBJECT TERMS Propeller, Tip Vortex, Cavitation			15. NUMBER OF PAGES 62	
			16. PRICE CODE	
17. SECURITY CLASSIFICATION OF REPORT UNCLASSIFIED	18. SECURITY CLASSIFICATION OF THIS PAGE UNCLASSIFIED	19. SECURITY CLASSIFICATION OF ABSTRACT UNCLASSIFIED	20. LIMITATION OF ABSTRACT	

THIS PAGE INTENTIONALLY LEFT BLANK

CONTENTS

SYMBOLS	v
ABSTRACT	1
ADMINISTRATIVE INFORMATION	1
INTRODUCTION	1
EXPERIMENTAL APPARATUS	2
Water Tunnel	2
Propeller.....	2
Laser Doppler Velocimetry System.....	2
Hybrid LDV System.....	4
Fiber-Optic LDV System.....	4
Seeding System	5
TEST CONDITIONS	5
COORDINATE SYSTEM.....	6
UNCERTAINTY ANALYSIS	7
Elemental Uncertainties.....	7
Calculated Uncertainties.....	8
Assessment of Model Propeller Geometry	10
RESULTS.....	10
Propeller Performance	10
Cavitation Performance	11
Cavitation Inception	11
Attachment Point and Trajectory.....	13
Circumferentially Averaged Velocities	13
Mean Velocity	14
Turbulence	15
Streamwise Vorticity	16
Variations in the Measurements	17
Blade-to-Blade Variation.....	17
Measurement Set Variation	17
Comparison of Velocity Measurements to Flow Models	18
CONCLUSIONS	18

FIGURES

Fig. 1. Propeller 5168, with fairwater.....	20
Fig. 2 Hybrid lens-optic/fiber-optic LDV system in the 36-inch water tunnel.....	21
Fig. 3 All fiber-optic LDV system in the 36-inch water tunnel.....	21
Fig. 4. The secondary-flow coordinate system.....	22
Fig. 5. Pitch-line perpendicular plane for secondary flow presentation.	22
Fig. 11. Propeller 5168 blade measurement matrix.	23
Fig. 13. Comparison of measured and design blade profiles.	24
Fig. 15. Estimated chord-length cutback from measured section offsets.	25
Fig. 17. Predicted minimum C_p variations due to geometry perturbations.....	25
Fig. 19. Performance of propeller 5168.....	26
Fig. 20. Propeller 5168 with cavitating tip vortices.....	26
Fig. 21. Tip-vortex cavitation inception for propeller 5168 vs. J	27
Fig. 22. Tip-vortex cavitation inception for propeller 5168 vs. K_T	27
Fig. 23. Location of attached tip vortex at $J = 0.98$ and 1.10	28
Fig. 24. Propeller 5168 tip-vortex trajectory.	29
Fig. 25. Circumferentially averaged velocity with dummy hub.	30
Fig. 26. Circumferentially averaged inflow velocity variation with J , $x/R = -0.4049$	31
Fig. 27. Circumferentially averaged velocity variation with J , $x/R = 0.2386$	32
Fig. 28. Circumferentially averaged velocity variation with x , $J = 1.10$	33
Fig. 29. Circumferentially averaged velocities, hybrid vs. fiber-optic data set, $J = 1.10$, $x/R = 0.2386$	34
Fig. 30. Circumferentially averaged velocity asymmetry, hybrid data set, $J = 1.10$, $x/R = 1.091$	35
Fig. 31. Propeller wake velocities in the stationary frame.....	36
Fig. 32. Contours of the streamwise velocity, with secondary flow particle traces.....	37
Fig. 33. Blade-to-blade variation of the tip vortex, contours of V_s/V_∞ with secondary flow vectors.....	38
Fig. 34. Contours of V_s/V_∞ downstream of the propeller, $J = 1.10$	39
Fig. 35. Development of the tip-vortex flow, moving downstream, $J = 1.10$	40
Fig. 36. Comparison of the tip-vortex region for differing advance coefficients, $x/R = 0.2386$	41
Fig. 37. Contours of q downstream of the propeller, $J = 1.10$	42
Fig. 38. Turbulence in the vortex, moving downstream, $J = 1.10$	43
Fig. 39. Turbulence in the vortex, $x/R = 0.2386$, $J = 1.10$, hybrid LDV system.	44
Fig. 40. Turbulence in the vortex, $x/R = 0.2386$, $J = 1.10$, fiber-optic LDV system.	45
Fig. 41. Contours of $\overline{V_s V_c}$, with cut at $r/R = 0.700$, $x/R = 0.2386$, $J = 1.10$	46

Fig. 42. Contours of $\overline{V_s V_c}$, with cuts through the vortex core, $x/R = 0.2386$, $J = 1.10$	47
Fig. 43. Streamwise vorticity in the tip-vortex region, $x/R = 0.2386$	48
Fig. 35. Streamwise vorticity in the tip-vortex region, $J = 1.10$	49
Fig. 36. Blade-to blade variation of ω_s , fiber-optic system, $x/R = 0.2386$, $J = 1.10$	50
Fig. 46. Comparison of ω_s from hybrid and fiber-optic systems, $x/R = 0.2386$, $J = 1.10$	51
Fig. 38. Comparison of V_θ from hybrid and fiber-optic systems, $x/R = 0.2386$, $J = 1.10$	52
Fig. 39. Comparison of V_{sn} from hybrid and fiber-optic systems, $x/R = 0.2386$, $J = 1.10$	53
Fig. 40. Comparison of calculated and measured circulation distribution.	54
Fig. 41. Comparison of measured and calculated blade wake pitch.	54

TABLES

Table 1. Propeller 5168 geometric parameters. Blade sections are non-standard.	3
Table 2. Measured flow conditions.	5
Table 3. LDV measurement planes.	5
Table 4. Elemental uncertainties.....	7
Table 6. Open water performance data for Propeller 5168.....	11
Table 7. Propeller 5168 tip-vortex inception and measured loads.....	12

SYMBOLS

C	Propeller chord length
C_p	Pressure coefficient, $1 - (V/V_\infty)^2$
D	Propeller diameter, 15.856 inches (402.7 mm)
F	Maximum blade section camber
i_t	Total blade rake
J	Propeller advance coefficient, U_∞/nD
K_Q	Torque coefficient, torque/ $(\rho n^2 D^5)$
K_T	Thrust coefficient, thrust/ $(\rho n^2 D^4)$
n	Propeller rotational speed, rev/s
P	Propeller pitch
p	Static pressure in tunnel

p_v	Vapor pressure of water
q	Root-mean-square (RMS) fluctuation of velocity, $\text{TKE} = q^2/2$, normalized by U_∞
r	Radius, normalized by R
R	Propeller radius, 7.928 inches (201.4 mm)
T	Maximum blade section thickness
Re	Blade Reynolds number, evaluated at $r = 0.7$, $[U_\infty^2 + (2\pi rn)^2]^{1/2} \cdot C / \nu$
U_r	Radial velocity in the measured (fixed) frame, positive outward, normalized by U_∞
U_t	Tangential velocity in the measured (fixed) frame, positive counterclockwise looking downstream, normalized by U_∞
U_x	Axial velocity in the measured (fixed) frame, positive downstream, normalized by U_∞
U_∞	Inflow velocity in the stationary frame (i.e., tunnel velocity)
V	Total velocity in the rotating frame
V_c	Cross-stream velocity in the rotating frame, normalized by U_∞
V_r	Radial velocity, normalized by U_∞ (identical to U_r)
V_s	Streamwise velocity in the rotating frame, normalized by U_∞
V_{sn}	Streamwise velocity in the rotating frame, normalized by V_∞
V_t	Tangential velocity in the rotating frame, positive counterclockwise looking downstream, normalized by U_∞
V_x	Axial velocity, normalized by U_∞ (identical to U_x)
V_θ	Secondary velocity magnitude $(V_c^2 + V_r^2)^{1/2}$
V_∞	Inflow velocity in the rotating frame $(U_\infty^2 + (2\pi rn)^2)^{1/2}$
x	Axial coordinate, from propeller mid plane
η	Propeller efficiency, $\frac{J}{2\pi} \frac{K_T}{K_Q}$
θ	Circumferential angle, radians
θ_s	Blade skew angle
ν	Kinematic viscosity

ρ	Density
σ_i	Cavitation number at cavitation inception, $\frac{p - p_v}{\frac{1}{2}\rho U_\infty^2}$
ϕ	Propeller pitch angle
ω_s	Streamwise vorticity, normalized by U_∞/R

THIS PAGE INTENTIONALLY LEFT BLANK

ABSTRACT

Detailed velocity measurements were made of the velocity field behind Propeller 5168 in the Carderock Division, Naval Surface Warfare Center (CDNSWC) 36-inch water tunnel. The measurements were made in order to examine the behavior of the tip-vortex flow. A first set of measurements was made with a three-component, non-coincident Laser Doppler Velocimeter (LDV) system at four different advance coefficients and at four downstream stations. A second set of measurements was made with a three-component, coincident LDV system at a single advance coefficient and downstream station. The coincident set of measurements was of higher accuracy and included data on the Reynolds shear-stress terms. Plots are presented of the detailed tip-vortex structure, and the variation of this structure with advance coefficient and location is examined. Data on the thrust, torque, and cavitation performance of the propeller are also included.

ADMINISTRATIVE INFORMATION

This report is submitted in partial fulfillment of milestone 3, Design/construct prop tips of subtask 2, Propeller Tip-Vortex Cavitation in the Advanced Propulsion Concepts Task. This is part of the Maneuvering and Seakeeping Project Area (R2133-MS3), in the Surface Ship Technology Program Plan (Program Element 060212N) for Fiscal Year 1998. The work described herein was sponsored by the Office of Naval Research (ONR 334) and performed by the Carderock Division of the Naval Surface Warfare Center, Code 5400 under Work Unit Number 1-5060-727.

INTRODUCTION

The Naval Surface Warfare Center is presently engaged in a joint project with the Royal Netherlands Navy and Marine Research Institute, Netherlands (MARIN) to develop propeller blade tip geometries that will improve tip-vortex cavitation. The program includes development of design procedures and geometries using potential-flow panel methods, Reynolds-Averaged Navier-Stokes (RANS) codes, and iterative propeller-model tests. To develop baseline data for a state-of-the-art combatant-type geometry, Propeller 5168 was selected for fundamental experiments to measure tip-vortex cavitation inception and near-tip velocity distributions in uniform inflow. All tests were performed in the CDNSWC 36-inch water tunnel.

Measurements were first made with a hybrid lens-optic/fiber-optic LDV system which measured all three components of velocity and the normal stresses, but did not measure the shear stresses. The first set of measurements was made at several advance coefficients and at several locations downstream of the propeller. After analysis of the first data set, it was decided to make a second set of measurements using an all fiber-optic LDV system. The fiber-optic system allowed for coincident velocity measurements to be obtained, which both increased the accuracy of the mean-velocity measurements and allowed for the measurement of the shear

stresses. The fiber-optic system had a much smaller effective measurement volume than the hybrid LDV system, which resulted in a lower data rate and longer data collection times. Therefore, the measurements with the fiber-optic system were obtained only at one advance coefficient and one downstream station.

The propeller, its performance, the flow about the propeller, and the instrumentation used will be described here; and the uncertainties involved in obtaining the data will be analyzed. Several plots of the data will be presented, but only at selected flow conditions. The entire data set is present in companion data files. The equations and techniques used to generate the plots will be presented here so that the reader may generate additional plots from the data set.

EXPERIMENTAL APPARATUS

Water Tunnel

All measurements were made in the David Taylor, 36-inch, Variable Pressure Water Tunnel. The tunnel is a recirculating design with interchangeable test sections. A 36-inch diameter, open-jet test section was used for these tests. The tunnel allows the pressure in the test section to be varied so that cavitation inception can be investigated. Both upstream and downstream drives are available for propeller testing. For these tests, the propeller was driven from upstream. Inflow to the propeller was uniform except for the wakes from the three upstream shaft support struts.

Propeller

The propeller used for this investigation is the David Taylor Propeller 5168, shown in Fig. 1. This is a five-bladed, controllable-pitch propeller with a design advance ratio, J , of 1.27. The propeller is left handed with a radius, D , of 15.856 inches (402.7 mm). A cylindrical fairwater 3.81" (96.8 mm) long was attached aft of the propeller hub. No boundary-layer tripping was employed. The geometry of the propeller is listed in Table 1.

Laser Doppler Velocimetry System

Two sets of LDV measurements were made with two different LDV systems. The first system was a hybrid lens-optic/fiber-optic system, and the second was an all fiber-optic system. The common elements of each system will be described in this section, while the specific elements of each systems will be described in their own sections.

Both systems utilized the blue (488nm), green (514.5nm), and violet (476.5nm) beams of an argon-ion laser to measure the radial, tangential, and axial velocity components, respectively. The measurement volume was positioned at a point in the horizontal plane containing the propeller axis. The probe volumes were translated in the axial and radial directions in order to get two directions of movement in the flow field, while the rotation of

the propeller relative to the measurement point provided the third direction of movement. The position of the shaft was encoded with an 8192 counts/revolution signal, which was recorded with each velocity measurement. The measurements are grouped into 1024 circumferential positions, each 8 encoder counts wide.

Table 1. Propeller 5168 geometric parameters. Blade sections are non-standard.

r/R	C/D	P/D	i/D	ϕ (deg.)	θ_s (deg.)	T/C	F/C
0.2819	0.18910	1.02029	0.01709	49.042	9.870	0.30984	-0.05404
0.3000	0.20000	1.08750	0.01110	49.086	6.280	0.26936	-0.03800
0.3500	0.23700	1.24479	-0.00694	48.545	-0.754	0.17804	-0.00860
0.4000	0.27600	1.36525	-0.02370	47.372	-4.824	0.11423	0.00903
0.4500	0.30800	1.45791	-0.03579	45.882	-7.336	0.08897	0.01779
0.5000	0.33410	1.54131	-0.04367	44.457	-8.865	0.07546	0.02789
0.6000	0.38540	1.67347	-0.04825	41.599	-9.838	0.05858	0.03655
0.7000	0.43500	1.63334	-0.04195	36.602	-8.108	0.04874	0.03323
0.8000	0.47450	1.50246	-0.03025	30.871	-3.784	0.04108	0.02473
0.9000	0.46500	1.33483	-0.01645	25.272	3.784	0.04376	0.01191
0.9500	0.39000	1.18919	-0.00960	21.725	9.297	0.05883	0.00539
1.0000	0.00000	0.90000	-0.00245	15.986	16.400	0.06222	0.00000
0.2900	0.19375	1.05108	0.01447	49.082	8.184	0.29115	-0.04639
0.3200	0.21388	1.15523	0.00401	48.969	3.007	0.22961	-0.02415
0.3400	0.22910	1.21647	-0.00329	48.715	0.364	0.19429	-0.01327
0.3600	0.24499	1.27163	-0.01054	48.351	-1.754	0.16265	-0.00427
0.3800	0.26086	1.32109	-0.01743	47.897	-3.449	0.13531	0.00326
0.4200	0.28978	1.40469	-0.02912	46.792	-5.970	0.10060	0.01299
0.4400	0.30222	1.44071	-0.03374	46.185	-6.923	0.09219	0.01613
0.4600	0.31352	1.47481	-0.03768	45.582	-7.709	0.08597	0.01968
0.4800	0.32400	1.50809	-0.04099	45.002	-8.349	0.08041	0.02386
0.5200	0.34424	1.57474	-0.04571	43.949	-9.273	0.07113	0.03113
0.5400	0.35448	1.60675	-0.04715	43.444	-9.577	0.06735	0.03351
0.5600	0.36478	1.63526	-0.04803	42.907	-9.773	0.06406	0.03514
0.5800	0.37510	1.65819	-0.04838	42.303	-9.861	0.06116	0.03612
0.6200	0.39562	1.67956	-0.04768	40.771	-9.704	0.05626	0.03654
0.6400	0.40574	1.67725	-0.04671	39.835	-9.461	0.05414	0.03613
0.6600	0.41570	1.66788	-0.04540	38.813	-9.112	0.05221	0.03541
0.6800	0.42547	1.65279	-0.04379	37.728	-8.660	0.05042	0.03442
0.7200	0.44421	1.61073	-0.03991	35.455	-7.457	0.04714	0.03188
0.7400	0.45296	1.58572	-0.03770	34.298	-6.704	0.04559	0.03038
0.7600	0.46108	1.55893	-0.03534	33.142	-5.845	0.04408	0.02870
0.7800	0.46835	1.53097	-0.03285	31.996	-4.872	0.04259	0.02682
0.8200	0.47913	1.47371	-0.02756	29.773	-2.571	0.03964	0.02242
0.8400	0.48161	1.44381	-0.02481	28.684	-1.223	0.03868	0.01993
0.8600	0.48104	1.41152	-0.02202	27.585	0.276	0.03870	0.01731
0.8800	0.47613	1.37560	-0.01923	26.454	1.940	0.04023	0.01462
0.9100	0.45626	1.31212	-0.01508	24.654	4.777	0.04639	0.01056
0.9200	0.44492	1.28705	-0.01371	24.004	5.823	0.04944	0.00923
0.9300	0.43054	1.25876	-0.01234	23.308	6.922	0.05267	0.00792
0.9400	0.41252	1.22642	-0.01098	22.553	8.079	0.05587	0.00664
0.9600	0.36169	1.14621	-0.00821	20.809	10.579	0.06132	0.00420
0.9700	0.32541	1.09665	-0.00681	19.792	11.927	0.06312	0.00305
0.9800	0.27696	1.03965	-0.00538	18.659	13.344	0.06402	0.00196
0.9850	0.24544	1.00811	-0.00466	18.045	14.080	0.06406	0.00144
0.9900	0.20562	0.97439	-0.00393	17.395	14.834	0.06379	0.00094
0.9950	0.15000	0.93839	-0.00320	16.710	15.607	0.06319	0.00046
0.9970	0.11805	0.92332	-0.00290	16.425	15.922	0.06285	0.00027
0.9980	0.09732	0.91565	-0.00275	16.280	16.081	0.06265	0.00018
0.9990	0.06966	0.90787	-0.00260	16.134	16.240	0.06244	0.00009
0.9995	0.04967	0.90395	-0.00252	16.060	16.320	0.06233	0.00005

Doppler signals were analyzed with a TSI Model IFA 655 Digital Burst Correlator. The processor performs a 256-sample, double-clipped, autocorrelation on each doppler burst, allowing the measurement of velocity even when the signal-to-noise ratio is low. The processors were operated in the random mode with the hybrid LDV system, and in the coincidence mode with the fiber-optic LDV system.

Hybrid LDV System

The hybrid LDV system consisted of both a lens-optic assembly and a fiber-optic probe assembly as shown in Fig. 2. The lens-optic system assembly measured two components of velocity and the fiber-optic assembly measured a single component of velocity. Each system was traversed independently.

The lens-optic assembly utilized the green (514.5 nm) and violet (476 nm) beams of an argon-ion laser to measure the tangential and axial components of velocity, respectively, in a 0.06×0.9 mm probe volume. The optics for this assembly were outside of the tunnel, and passed through a window into the water. A special insert in the open-jet test section was used to place the front lens of the assembly closer to the propeller than would normally be possible. The insert extended in the test section to just outside the open jet. This both decreased the size of the probe volume and increased the signal-to-noise ratio. The assembly was mounted on a three-component traverse.

The fiber-optic probe utilized the blue (488 nm) beam of the argon-ion laser to measure the radial component of velocity in a 0.07×1.3 mm probe volume. The fiber-optic probe was placed inside the test section, below the plane of measurements. The probe was mounted on a traverse which could be moved in both the axial and radial directions.

Because of the two separate traverses, it was difficult to keep all three measurement volumes precisely coincident. The processors were therefore operated in random mode, and Reynolds shear stress data were not acquired. Reynolds normal stresses, however, were acquired.

Fiber-Optic LDV System

The fiber-optic LDV system consisted of two TSI model 9832 fiber optic probes as shown in Fig. 3. The two probes were rigidly mounted together on a traverse which could translate in the axial and radial directions. The focal distance of the probes (470 mm in water) was sufficient to place the probe bodies outside of the jet.

The horizontal probe utilized the green (514.5 nm) and violet (476 nm) beams of an argon-ion laser to measure the tangential and axial components of velocity, respectively. The vertical probe utilized the blue (488 nm) beam of the argon-ion laser to measure the radial component of velocity. Both probe volumes were 0.07×1.3 mm.

Table 2. Measured flow conditions.

J	n (RPM)	U_{∞} (ft/s, m/s)	T (lbf., N)	Q (ft·lbf, N·m)
0.98	1200	25.90, 7.89	860, 3826	277, 376
1.10	1450	35.10, 10.70	1060, 4715 (1075, 4782)	355, 481 (365, 495)
1.27*	1300	36.35, 11.08	580, 2580	222, 301
1.51	1150	38.49, 11.73	150, 667	90, 122

Values in parentheses for fiber-optic system.

*design condition

With the probes mounted rigidly together, it was possible to keep the measurement volumes precisely aligned, and the processors were operated in coincidence mode. This allowed shear stresses to be measured and velocity bias corrections to be applied to the measurements. This also reduced the effective probe volume to 0.07×0.07 mm.

Seeding System

The flow was seeded with silicon-carbide powder. Since the water in the tunnel recirculates, seed needed to be added only infrequently.

TEST CONDITIONS

Velocity measurements were performed at the four advance ratios listed in Table 2. All measurements were at an approximate water temperature of 75°F. It was not possible to exactly match the flow conditions of the hybrid test when the fiber-optic test was performed. The values in parentheses at $J = 1.10$ are for the fiber-optic LDV system, while the other values are for the hybrid system. This mismatch will be discussed further in the *Results* section. Tip-vortex cavitation could be observed at the two lowest advance ratios, but none was observed at the two highest advance ratios. Pressure was kept high enough during the LDV measurements to suppress cavitation, since the presence of cavitation bubbles would interfere with the propagation of the laser beams through the water.

Table 3. LDV measurement planes.

J	x/R				
	-0.4049	0.1756	0.2386	0.3963	0.8378
0.98	N		N		
1.10	NC	N	NC	N	N
1.27	N		N		
1.52	N		N		

N - Non-coincident measurements acquired

C - Coincident measurements acquired

Velocity measurements were obtained both upstream and downstream of the propeller, as detailed in Table 3. At all advance coefficients, measurements were made at an upstream location — $x/R = -0.4049$, as measured from the propeller mid plane — and a downstream location — $x/R = 0.2386$. Coincident measurements were made only at these two planes, and only for $J = 1.10$. Non-coincident measurements were made at these two planes for four advance coefficients — $J = 0.98, 1.10, 1.27$, and 1.52 — and at additional downstream locations for $J = 1.10$. At the downstream locations, the radial increment between measurements was $0.1R$ over most of the span, with a radial increment of 0.02 to $0.03R$ in the region of the tip vortex. At the condition of $J = 1.10$, $x/R = 0.2386$, measurements were spaced in a denser grid. At $J = 1.10$, $x/R = 0.1756$, only the tip region of the flow could be measured, due to blockage of the laser beams by the propeller.

COORDINATE SYSTEM

The measurements in the data file are all normalized by the tunnel velocity, U_∞ , and are presented in the rotating frame. The relation between the stationary (measured) frame velocities, U , and the rotating frame velocities, V , is:

$$\begin{aligned} V_x &= U_x \\ V_t &= U_t - 2\pi r n \\ V_r &= U_r \end{aligned} \tag{1}$$

The measurements in the plots are presented in a primary/secondary coordinate system in order to highlight the vortex structure. In this coordinate system, illustrated in Fig. 4, the primary velocity, V_s , is defined as being in the axial-tangential plane, at the propeller pitch angle. The secondary velocities are then the orthogonal velocity component in the $x-t$ plane, V_c , and the radial velocity, V_r . Since the pitch angle is different at each radius, the coordinate system is different at each radius as well. These velocity components can be calculated from:

$$V_s = V_x \sin \phi + V_t \cos \phi \tag{2}$$

$$V_c = -V_x \cos \phi + V_t \sin \phi \tag{3}$$

$$V_r = V_r \tag{4}$$

Similarly, the velocity-stress terms can be calculated from:

$$\overline{V_s^2} = \overline{V_x^2} \sin^2 \phi + 2\overline{V_x V_t} \sin \phi \cos \phi + \overline{V_t^2} \cos^2 \phi \tag{5}$$

$$\overline{V_c^2} = \overline{V_x^2} \cos^2 \phi - 2\overline{V_x V_t} \sin \phi \cos \phi + \overline{V_t^2} \sin^2 \phi \tag{6}$$

$$\overline{V_r^2} = \overline{V_r^2} \tag{7}$$

$$\overline{V_s V_c} = \frac{1}{2} (\overline{V_t^2} - \overline{V_x^2}) \sin 2\phi - \overline{V_x V_t} \cos 2\phi \tag{8}$$

$$\overline{V_s V_r} = \overline{V_x V_r} \sin \phi + \overline{V_t V_r} \cos \phi \quad (9)$$

$$\overline{V_c V_r} = -\overline{V_x V_r} \cos \phi + \overline{V_t V_r} \sin \phi \quad (10)$$

The secondary flow components thus defined are perpendicular to the propeller pitch line. In order to examine vectors of the secondary flow — particularly in the tip-vortex region — it is therefore useful to adjust the aspect ratio of the plot to make the vortex appear as if it were measured in a plane perpendicular to the blade pitch line, as shown in Fig. 5. To do this, the angular coordinate for each plotted point is found from:

$$\theta_p = (\theta - \theta_c) \sin \phi \quad (11)$$

where θ is the actual circumferential coordinate, θ_p is the plotted circumferential coordinate, θ_c is the circumferential coordinate of the center of the plot, and ϕ is the propeller pitch angle (note that ϕ is a function of r). This makes the cross section of the vortex circular and makes the secondary-flow vectors point in the correct direction.

UNCERTAINTY ANALYSIS

The uncertainties for some terms are different for the hybrid LDV system and for the fiber-optic LDV system. Where the uncertainties are different for the two systems, the text will explicitly state so, and the tables will list the uncertainty for the hybrid system normally, with the uncertainty for the fiber-optic system following italicized in parentheses.

Elemental Uncertainties

The uncertainties for the fundamental quantities measured in this experiment are listed in Table 4. Those uncertainties which are the same for all measurements are listed as bias uncertainties, and those uncertainties which vary for each measurement are listed as precision uncertainties. Uncertainties are listed as a fraction of the nominal value, unless otherwise noted.

Table 4. Elemental uncertainties.

Item	Bias	Precision	Item	Bias	Precision
U_∞	0.005	0.003	$\Delta x (V_x - V_t)$	0.00015 <i>R</i>	(0)
n	0.00008	0.00014	$\Delta t (V_x - V_t)$	0.0015 <i>R</i>	(0)
d_f	0.003		$\Delta r (V_x - V_t)$	0.00015 <i>R</i>	(0)
x	0.0005 <i>R</i>		$\Delta x (V_t - V_r)$	0.0003 <i>R</i>	(0)
t	0.0015 <i>R</i>		$\Delta t (V_t - V_r)$	0.004 <i>R</i>	(0)
r	0.0015 <i>R</i>		$\Delta r (V_t - V_r)$	0.003 <i>R</i>	(0)
θ		0.05°			

Note: Where uncertainties for the hybrid and fiber-optic systems differ, the fiber-optic uncertainty is listed in parentheses.

The uncertainties in x , t , and r are the uncertainties in positioning the probe volume with respect to the propeller. The Δx , Δt , and Δr uncertainties are the uncertainties in positioning the three probe volumes with respect to each other. Since coincidence between the probe volumes is ensured by the coincidence mode of the processor, this uncertainty is zero for the fiber-optic system. Uncertainty in the measurement of the frequency is assumed to be small relative to the uncertainty due to finite sample size, and so is ignored. The uncertainty in the perpendicularity of the three measured components is assumed to be small compared to the uncertainty in fringe spacing and probe volume coincidence, and is ignored as well.

Calculated Uncertainties

The calculated uncertainties for the quantities found by combining other measurements are presented in Table 5. The calculation of the uncertainty in J from the uncertainties in Table 4 is straight forward. However, the rest of the items in Table 5 can only be calculated with information on the local flow conditions. This is because all of these items depend on the values of the velocity, velocity gradients, or turbulence intensity. The uncertainties in Table 5 are therefore listed for two representative flow conditions. The first, case 1, is a point in the "inviscid" flow between the blade wakes. In this region, the turbulence intensity is low and the flow gradients are small. Case 1 is representative of the majority of the flow. For case 1, the benefits of operating the LDV system in coincidence mode are minimal, and the uncertainties in this region are essentially the same for the hybrid and all fiber-optic measurements. Case 2 is a point in the tip vortex. At this location the turbulence intensity and the velocity gradients are at their highest values, and so the uncertainties are a

Table 5. Calculated uncertainties.

Item	Case 1 (Inviscid Flow)			Case 2 (Tip Vortex)			Reference
	Bias	Precision	Total	Bias	Precision	Total	
J	0.005	0.003	0.006	0.005	0.003	0.006	J
U_x, V_x	0.003	0.002	0.004	0.18 (0.003)	0.03	0.19 (0.03)	U_∞
U_t	0.001	0.001	0.002	0.074 (0.002)	0.015	0.075 (0.015)	U_∞
U_r, V_r	0.0003	0.001	0.001	0.18 (0.001)	0.03	0.19 (0.023)	U_∞
V_t	0.001	0.001	0.002	0.074 (0.002)	0.015	0.075 (0.015)	U_∞
V_s	0.002	0.002	0.003	0.10 (0.002)	0.02	0.11 (0.019)	U_∞
V_c	0.003	0.002	0.004	0.17 (0.003)	0.03	0.17 (0.028)	U_∞
V_v	0.003	0.002	0.004	0.17 (0.003)	0.03	0.17 (0.028)	U_∞
q	0.00	0.10	0.10	0.25 (0.00)	0.10	0.10 (0.027)	q
$V_x V_t \dots$	0.0000	0.0001	0.0001	0.0000	0.003	0.003	U_∞^2
$V_s V_c \dots$	0.0001	0.0001	0.00015	0.0000	0.003	0.003	U_∞^2
ω_s				0.4 (0.15)	0.13	0.42 (0.20)	ω_s

Note: Where uncertainties for the hybrid and fiber-optic systems differ, the fiber-optic uncertainty is listed in parentheses.

maximum. Case 2 is representative of only a very small fraction of the flow, but the fraction of most interest. For case 2, the severe flow gradients make precise alignment of the measurement volumes essential, and the accuracy of the hybrid system suffers as a result.

For case 1, the velocity uncertainties are all below 0.5% of the inflow velocity. In this region of the flow, the velocity uncertainty is dominated by the uncertainty in the fringe spacing of 0.3%. Flow gradients in this region are small, so the uncertainties for the two LDV systems are identical.

For case 2, the uncertainties are higher due to a number of effects. The precision uncertainty is higher than in case 1 due to the uncertainty in finding the mean in a high turbulence region with a relatively small sample size (~250). The bias uncertainty is higher due to two effects. First, the high turbulence intensity causes there to be a bias in the average velocity towards fluid traveling with a higher total velocity, due to the correlation between particle arrival rate and fluid velocity. In a highly three-dimensional flow, this can be corrected using knowledge of the correlation between the different velocity components, so this adds uncertainty only to the measurements with the hybrid LDV system. Second, the high gradients in velocity combine with the uncertainty in probe-volume coincidence to give a bias uncertainty in velocity. This is the dominant source of velocity uncertainty for the hybrid system. It is not present for V_x , since it is assumed that the measurement volume for that component is the probe position, and errors in probe volume coincidence are relative to that volume.

Precision uncertainty in the measurement of the turbulent velocity fluctuations, q , is dominated by the uncertainty in finding the variance of a distribution with a finite sample size. For a sample size of 250, that uncertainty is approximately 10%. Bias in the turbulence intensity measurements arises due to non-coincidence of the probe volumes, and so is only present for the hybrid measurements. It should be noted, however, that the LDV has a lower noise floor, below which it can not measure the turbulence. For this setup, the noise floor in q was approximately 1.5% of the measured velocity.

Uncertainties for the Reynolds shear stress terms apply only to the fiber-optic measurements, since only those measurements yielded the shear stress terms. The row labeled $V_x V_y$ contains the uncertainties for the *measured* shear stress terms, while the row labeled $V_x V_z$ contains the uncertainties for the *transformed* shear stress terms. The precision uncertainty for these terms comes from the statistical uncertainty resulting from the relatively small sample size. Bias in the measured terms is small, but some bias is introduced to the transformed terms due to the inability of the system to measure a zero normal stress.

Uncertainty in the magnitude of the streamwise vorticity was difficult to estimate analytically. The effect of velocity bias on the streamwise vorticity was estimated by multiplying the measured velocities by $(1 + q^2/U^2)^{-1}$, where U is the velocity magnitude in the fixed (measured) frame, and recalculating the vorticity. The change in

streamwise vorticity was on the order of only 3%. The effect of other sources of uncertainty was quantified by analyzing variations in vorticity between differing blades and between different measurement sets. The numbers found from this analysis were much higher than 3%, and are listed in Table 5. Uncertainty for the hybrid system is much higher than for the fiber-optic system due to the possible misalignment of the probe volumes. No uncertainty is listed for case 1 (the inviscid region) since ω is near zero in this region.

Uncertainty in the inception cavitation number was primarily a precision uncertainty. From the inception data scatter over all the measurements taken, uncertainty in σ_i was estimated as ± 0.4 .

Assessment of Model Propeller Geometry

Model Propeller 5168 was manufactured using numerical control milling techniques, representing state-of-the-art model manufacturing. To assess the accuracy of the model, each of the five blades was measured at $r = 0.32, 0.34, 0.5, 0.7, 0.9, 0.95, 0.97, \text{ and } 0.98$. The measurement points are shown in Fig. 6. Fig. 7 shows comparisons of the design and measured blade profiles. Fig. 7a shows a problem area near the tip, where the leading edge was “cut back” relative to the design offsets. Fig. 7b shows a typically good match between the design and measured geometry, showing a slight pitch deviation, which was typical over most of the blade.

An attempt was made to quantify the effects of the deviations documented in the geometry measurements. Calculations were performed with the panel code with estimated geometry deviation. The leading edge cut back was modeled by assuming a chord length shortening as shown in Fig. 8. The assumed shortening is compared to Navy full scale tolerances on chord length. Also, the effect of pitch deviation was estimated by assuming a uniform pitch error of 0.7% across the span of the blade. Fig. 9 shows the results of the panel calculations. The deviations affected the minimum pressure at the blade tip up to a C_p - value of 0.2. This was about half the estimated error in the measurement of the tip-vortex cavitation inception number. It should be acknowledged that the panel code is not capable of accurately calculating the C_p associated with tip-vortex inception, but it may be capable of predicting relative values when perturbing geometry.

RESULTS

Propeller Performance

Initially, propeller 5168 was operated at high tunnel pressure to suppress cavitation and run at 30 ft/s over a range of J to determine the thrust and torque “open-water” performance. The propeller had been open-water tested earlier in the CDNSWC towing basin, with results tabulated in Table 6. Fig. 10 shows good comparison of the basin result and the measurements in the 36-inch water tunnel, thus validating the open flow characteristics of the open jet test section of the 36-inch water tunnel. Cavitation inception conditions could then be related to either thrust loading (K_T) or tunnel velocity (J).

Table 6. Open water performance data for Propeller 5168.

J	K_T	$10 \cdot K_Q$	η_0	J	K_T	$10 \cdot K_Q$	η_0
0.00	0.921	1.840	0.000	0.85	0.436	0.997	0.592
0.05	0.890	1.769	0.040	0.90	0.411	0.956	0.616
0.10	0.859	1.704	0.080	0.95	0.386	0.914	0.639
0.15	0.828	1.642	0.120	1.00	0.361	0.871	0.660
0.20	0.798	1.585	0.160	1.05	0.337	0.828	0.680
0.25	0.768	1.530	0.200	1.10	0.313	0.783	0.699
0.30	0.739	1.478	0.239	1.15	0.288	0.737	0.716
0.35	0.710	1.429	0.277	1.20	0.264	0.689	0.731
0.40	0.681	1.381	0.314	1.25	0.239	0.639	0.743
0.45	0.652	1.335	0.350	1.30	0.213	0.586	0.753
0.50	0.624	1.291	0.385	1.35	0.187	0.531	0.757
0.55	0.596	1.247	0.418	1.40	0.160	0.471	0.754
0.60	0.569	1.204	0.451	1.45	0.131	0.408	0.740
0.65	0.541	1.162	0.482	1.50	0.100	0.339	0.703
0.70	0.515	1.121	0.511	1.55	0.067	0.265	0.623
0.75	0.488	1.080	0.540	1.60	0.031	0.185	0.430
0.80	0.462	1.039	0.566				

Cavitation Performance

Fundamental cavitation inception tests were performed in the 36-inch water tunnel. The propeller was driven from upstream and run over a range of speeds and advance coefficients to identify the inception of suction and pressure-side tip-vortex cavitation.

Cavitation Inception

During cavitation tests, air content was maintained within a range of 60-80%, as has been the standard procedure for the 36-inch water tunnel at CDNSWC. Fig. 11 shows the propeller configuration with tip-vortex cavitation. Cavitation inception was determined by initially operating the propeller at a condition of no cavitation, then increasing propeller rpm until tip-vortex cavitation occurred. Inception was noted when three of the five blades showed intermittent tip-cavitation events at a rate of one event in ten seconds when observed with strobe illumination. Blade Reynolds number at inception ranged from 3.2 to 5.7×10^6 .

Fig. 12 and Fig. 13 show the tip-vortex cavitation inception results, which are also listed in Table 7. Typical behavior is seen for suction-side and pressure-side tip-vortex cavitation. Suction-side cavitation was observed relatively far downstream, approximately one-half rotation of the blade, at high loading (low J). At low loading ($J > 1.1$) the inception was observed closer to the blade, typically within 2 inches (50 mm) of the tip. Slight differences were seen at the two static pressures at which suction side tip-vortex cavitation was observed. The lower σ_i observed at the lower speeds and static pressures is qualitatively consistent with Reynolds number scaling.

Table 7. Propeller 5168 tip-vortex inception and measured loads.

Measured in the 36-inch water tunnel, uniform flow, 67°F, air content=70% at atmospheric pressure.

Table 7a. Suction-side tip vortex, $p = 22$ psia

J	V (ft/s)	n (rps)	K_T	$K_Q \times 10$	η	σ_i	$Re \times 10^{-6}$
0.921	21.51	17.68	0.392	0.926	0.620	6.94	2.92
0.983	25.76	19.83	0.364	0.876	0.651	4.80	3.31
0.992	27.75	21.18	0.364	0.871	0.660	4.14	3.54
1.034	30.32	22.20	0.344	0.845	0.671	3.51	3.74
1.055	32.37	23.22	0.332	0.818	0.682	3.07	3.93
1.062	32.73	23.33	0.327	0.805	0.685	3.01	3.95
1.066	35.69	25.35	0.329	0.813	0.686	2.53	4.29
1.082	36.69	25.67	0.315	0.787	0.690	2.39	4.36
1.102	39.78	27.33	0.305	0.770	0.695	2.02	4.66
1.103	37.65	25.85	0.302	0.765	0.693	2.27	4.41
1.116	39.55	26.83	0.300	0.754	0.707	2.06	4.59
1.117	43.08	29.20	0.304	0.757	0.714	1.72	4.99
1.130	42.53	28.50	0.296	0.747	0.712	1.78	4.88
1.134	44.45	29.68	0.291	0.737	0.713	1.61	5.09
1.155	50.40	33.04	0.280	0.716	0.719	1.25	5.69
1.191	52.01	33.07	0.259	0.675	0.728	1.17	5.73

Table 7b. Suction-side tip vortex, $p = 16.5$ psia

J	V (ft/s)	n (rps)	K_T	$K_Q \times 10$	η	σ_i	$Re \times 10^{-6}$
1.004	25.01	18.85	0.349	0.852	0.654	3.86	3.16
1.059	31.52	22.53	0.322	0.806	0.674	2.43	3.81
1.115	35.13	23.85	0.299	0.755	0.703	1.95	4.08
1.136	38.76	25.83	0.290	0.736	0.714	1.60	4.43
1.159	43.18	28.21	0.278	0.710	0.722	1.29	4.86
1.205	50.77	31.90	0.241	0.653	0.707	0.93	5.55

Table 7c. Pressure-side tip vortex, $p = 22$ psia

J	V (ft/s)	n (rps)	K_T	$K_Q \times 10$	η	σ_i	$Re \times 10^{-6}$
1.494	46.74	23.69	0.089	0.312	0.678	1.47	4.37
1.549	43.97	21.48	0.055	0.235	0.571	1.66	4.01
1.555	39.95	19.44	0.053	0.230	0.571	2.02	3.63
1.584	39.09	18.68	0.034	0.182	0.467	2.10	3.51

Pressure-side tip-vortex cavitation was observed emanating from pressure-side leading-edge cavitation. No coherent pressure-side vortex structure was observed. At CDNSWC, any pressure-side cavitation seen outboard of the 0.95 radius is normally categorized as pressure-side tip-vortex cavitation. This has important implications for scaling. CDNSWC standard practice is to scale both pressure-side tip-vortex cavitation and suction-side cavitation with Reynolds number. Leading-edge sheet cavitation is not scaled. Since, for this propeller, a vortex structure is not observed, scaling of the pressure-side tip vortex is questionable. Scaling pressure-side

tip-vortex cavitation could result in conservative pressure-side tip-vortex performance, and a restriction of design space.

Attachment Point and Trajectory

Over the range of J tested, suction-side tip-vortex attachment occurred aft of the blade tip. The attachment location was determined by reducing pressure until the tip vortex was persistent enough to, at least intermittently, attach to the blade. Fig. 14a shows a photograph of blade number 1 tip with the location of the tip-vortex attachment at $J = 1.1$ (labeled 1 in the photo) and $J = 0.98$ (labeled 2 in the photo). Fig. 14b shows the attachment points for all five blades at the two J conditions. The average location at $J = 0.98$ was the blade trailing edge at 0.997 radius, while at $J = 1.1$, the attachment point moved aft to 0.998 radius trailing edge. The blade-to-blade variation of the attachment location can be seen.

The pitch angle and radial location of the cavitating tip vortex was also observed. Using a sighting telescope attached to an angular measurement device, the pitch angle of the cavitating vortex was tracked from the blade tip to an axial location of approximately one diameter downstream. The radial location of the vortex was tracked using the LDV beam crossing point and the LDV traverse. Fig. 15 shows the result of these measurements. The maximum tip-vortex pitch occurred at $x/R = 0.4$, with the pitch and radius becoming constant downstream of $x/R = 1.6$.

Circumferentially Averaged Velocities

The nominal flow velocity (with a dummy hub, but without the propeller) is shown in Fig. 16. The axial velocity drops off below $r = 0.5$ due to the boundary layer along the shaft. There is a slight excess of axial velocity from $0.6 < r < 0.9$, with the flow at $r > 0.9$ being very close to the nominal tunnel velocity, U_∞ . This figure also shows that there is a small negative tangential velocity throughout the flow.

The flow velocity upstream of the propeller at $x/R = -0.4049$ is shown in Fig. 17. The effect of J is quite clear in the plots of U_x and U_r . Increasing loading of the propeller (decreasing the advance coefficient) causes the flow upstream of the propeller to accelerate and contract. The effect on U_t is negligible, however. In all cases the tangential velocity is very close to that measured with no propeller in the flow.

The measured circumferentially averaged velocities at $x/R = 0.2386$ at varying J are shown in Fig. 18. This figure shows that as loading increases (J decreases), the magnitude of all velocity components increases. At the tip, all U_x approaches 1 and U_t and U_r approach zero, although U_r approaches slowly.

The measured circumferentially averaged velocities at $J = 1.10$ at varying distance downstream are shown in Fig. 19. The greatest differences in the flow are seen in the tip region, where the high velocity gradients close to the blade weaken as the flow progresses downstream. Inside of the tip region, the axial velocity increases at

the downstream stations due to the contraction of the flow. The tangential velocity in this region then increases slightly, again due to the flow contraction.

A comparison between the measurements made with the hybrid system and measurements made with the fiber-optic system is shown in Fig. 20. As was noted in the *Test Conditions* section, it was not possible to precisely match the torque and thrust of the earlier set of measurements when the fiber-optic measurements were taken. Thrust was 1.4% higher for the fiber-optic measurements, and torque was 2.8% higher. This is reflected in the circumferentially averaged velocities shown in Fig. 20.

Measurements were made of the velocity at $x/R = 1.091$ across the propeller diameter using a long-focal-length, lens-optic LDV system. These measurements, shown in Fig. 21, show that there was a slight asymmetry in the flow with the window present. Axial velocity matches well on both sides of the tunnel centerline, but tangential velocity was slightly lower on the side away from the window insert than near it. It is believed that the discrepancy in flow conditions between the two sets of measurements is due to the window insert which was present for the hybrid measurements and not present for the fiber-optic measurements. Unfortunately, it was not possible to make similar measurements across the diameter of the propeller without the insert present. Whatever the cause of the differing flow conditions for the hybrid and fiber-optic measurements, it should be noted that the measurement sets are at slightly different conditions.

Mean Velocity

The velocity profiles at two radii in the “as collected” stationary frame are shown in Fig. 22. Fig. 22a, shows the profiles at $r = 0.70$. The spikes in the profiles result from the blade wake. Fig. 22b shows the velocity profile through the tip-vortex core at $r = 0.92$. In this figure, the profiles are more complex, with the features arising both from the vortex and the blade wake. Plotted in this manner, it is difficult to discern which features are associated with which structure. These features are easily identified, however, when the measurements at all radii are integrated into a single plot, with the measurements represented as contours and vectors.

Fig. 23 shows contours of the streamwise velocity normalized by the *relative* inflow velocity, $V_{sn} = V_s/V_\infty$, at $x/R = 0.2386$, $J = 1.10$ for all five blades of the propeller. This figure shows measurements taken with the fiber-optic system; the plot using the hybrid system data is nearly identical. The blade numbers are marked on the figure. In this plot the wakes are clearly visible as the curving green “spokes” in the plot of low velocity. (Note that the slight lumpiness is an artifact of the interpolation required to generate the contours in regions where the grid aspect ratio is very large). At the outer edge of the wakes are the tip vortices, also of low streamwise velocity. Superimposed on the contours are streamtraces of the secondary flow. These clearly show the circulation of flow around the tip vortex, as well as the radial flow generated by the blade wake. The

streamtraces also show a recirculating region between the blade tips; plots of the magnitude of the secondary flow velocity (not shown here) show these structures to be of much lower energy than the tip vortices.

Fig. 24 shows expanded plots of the tip vortices shown in Fig. 23. In this figure, the aspect ratio of the plots has been adjusted as explained in the *Coordinate System* section, and each vortex has been rotated to the same orientation and scaled identically. As can be seen in Fig. 24, the structure of the vortex and the velocity deficit in the core is nearly identical for the different blades. The position of the core, however, varies slightly from blade to blade — presumably due to slight variations in blade geometry. It is therefore recommended that any comparisons of the data to calculated flowfields be performed only after the core positions have been aligned.

A composite figure of all the measured downstream planes for $J = 1.10$ is shown in Fig. 25. In this figure, the contours again show the magnitude of V_s/V_∞ . For clarity, one blade has been removed from the figure, and a streamtube has been drawn to visually connect the measured vortex cores. This figure clearly shows the rapid decay and stretching of the wake and the separation of the wake from the vortex as the flow moves downstream.

Fig. 26 shows an expanded view of the tip vortex (again, with adjusted aspect) at the four downstream stations with contours of the magnitude of the secondary velocity, $V_\theta = \sqrt{V_c^2 + V_r^2}$. The strong asymmetry of the vortex can be seen here. Particularly close to the blade, the wake interacts with the tip vortex, damping the magnitude of the secondary flow on the wake side. It can also be seen that the secondary flow about the vortex has decayed little by the last measurement station. Some of the “lumpiness” in these plots is due to the non-alignment of the measurement components with the hybrid LDV system. This will be more closely examined in the *Turbulence* subsection.

Fig. 27 is a plot of the secondary velocity in the tip region for the four measured advance coefficients at the $x/R = 0.2386$ plane. This plot shows the decrease in vortex strength with increasing J , until at $J = 1.52$, nothing which classified as a vortex exists. These plots make it clear why no tip-vortex cavitation could be observed at the two highest advance coefficients.

Turbulence

Fig. 28 is identical in configuration to Fig. 25, but with contours of the RMS velocity fluctuations. This figure shows that the turbulence in the blade wake rapidly decreases as the flow moves downstream. Fig. 29 shows expanded plots of the vortex regions shown in Fig. 28. The figure shows that, although the region of high turbulence around the vortex becomes larger as the flow moves downstream, the peak value of turbulence in the vortex does not change.

The lobes of turbulence at the vortex core shown in Fig. 29 appear to be an artifact of the measurements rather than a part of the flow. This can be better seen in Fig. 30, where the RMS turbulence is shown broken into its three measured parts. The non-coincidence of the three probe volumes results in the peaks in the three turbulence components not occurring in the same location.

The measurements at the same location with the fiber-optic system, shown in Fig. 31, do not show this problem; the turbulence components in the vortex reach a maximum around the same point. The fiber-optic measurements do still show some lobes in the turbulence contours, however. The RMS turbulence reaches a maximum on either side of the vortex core in these measurements, with the peaks being at approximately 90° to one another for the axial and radial components. It is not clear if these lobes are due to non-isotropy in the flow turbulence, or due to some unknown measurement bias.

Measurements of the $\overline{V_s V_c}$ shear stress behind blade 3 are shown in Fig. 32. The figure also includes a plot of the turbulence terms on a cut through the plot at $r/R = 0.700$. The cut is shown at this radius since the radial velocity is near zero on both sides of the wake here, and the cut should show profiles similar to the wake behind a two-dimensional foil. (The radial velocity is, however not zero in the wake; it is positive outward.) The shear stress is, as expected, near zero throughout most of the passage. On the suction side of the wake (the bottom in Fig. 32), the streamwise-crosstream shear stress is negative, while on the pressure side the shear stress is positive. This is more easily seen from the cut through the plot. As would be expected for a 2-D wake, all the shear stresses are zero at the center of the wake. Both $\overline{V_s V_c}$ and $\overline{V_c V_r}$ change sign through the wake, but $\overline{V_s V_r}$ is negative on both sides of the wake.

Fig. 33 is an expanded view of the tip-vortex region of Fig. 32. In this figure, two cuts through the vortex are shown — one in the radial direction and one in the circumferential direction. The RMS turbulence in the radial cut shows a double peak, while in the circumferential cut shows a single peak. As was mentioned earlier, it is not clear if this reflects an actual minimum in turbulence near the vortex core or some measurement bias. The secondary velocity, V_θ , is substantially smaller on the side of the vortex towards the wake, reflecting the wake/vortex interaction. The dominant shear stress in the vortex region is $\overline{V_c V_r}$, which is what would be expected for an isolated vortex with minimal streamwise-velocity gradients.

Streamwise Vorticity

The streamwise vorticity was calculated as that component of the vorticity in the direction of V_s as defined earlier. In the s - c - r coordinate system (streamwise, cross-stream, radial), the streamwise vorticity is calculated from:

$$\omega_s = \frac{\partial V_r}{\partial c} - \frac{\partial V_c}{\partial r} \quad (12)$$

The measurements are, however, not in the c - r plane, but rather in the t - r plane. To evaluate the cross-stream derivative, the substitution

$$\frac{\partial}{\partial c} = \frac{1}{r \sin \phi} \frac{\partial}{\partial \theta} \quad (13)$$

is used. The results of these calculations are shown in Fig. 34 through Fig. 37.

Fig. 34 shows the streamwise vorticity for the four measured advance coefficients at $x/R = 0.2386$. The tip vortices for this prop spin in the counter-clockwise direction, looking downstream, and so the vorticity in the tip regions is negative. In Fig. 34, the large decrease in tip streamwise vorticity is seen with increasing J . At $J = 0.98$, the peak vorticity is approximately $-375 U_\infty / R$, at $J = 1.10$, that value is down to approximately -200 , and at $J = 1.52$, the tip vorticity has disappeared.

Fig. 35 shows the streamwise vorticity for the four axial locations measured at $J = 1.10$. In this figure, a line has been plotted at $r/R = 0.90$ to show how the vortex moves radially as the flow moves downstream. In Fig. 35, it can be seen that, though the tip vortex separates from the wake as the flow moves downstream, the strength of the vortex remains intact. The peak vorticity in the four locations varies from about -225 to $-170 U_\infty / R$. The variation of streamwise vorticity is not monotonic with x , and is therefore believed to be due to the uncertainties in the calculation of ω_s , and not representative of changes in the actual vortex strength.

Variations in the Measurements

Blade-to-Blade Variation

The blade-to-blade variation in V_{sn} , shown in Fig. 24, is small. However, the variation in some of the other quantities can be significant. Blade-to-blade variation in the fiber-optic measured streamwise vorticity is shown in Fig. 36. Peak vorticity varies from $-420 U_\infty / R$ for blade 4 to $-590 U_\infty / R$ for blade 5. It is believed that this variation is not a measurement artifact, since there are clearly differences in the cavitation inception among the blades and nearly identical variation is seen in the measurements made with the hybrid system.

Measurement Set Variation

The magnitude of the vorticity measured with the two LDV systems is considerably different. Fig. 37 shows the streamwise vorticity measured for blades 3 and 5 for both the fiber-optic and hybrid systems. Some of this variation is likely due to the slight variation in flow conditions for the two measurement sets, but the majority of the difference appears to be due to the inability to measure strong flow gradients as well with the hybrid system as with the fiber-optic system. As was shown with the turbulence components in Fig. 30 and Fig. 31, the measurement volumes for the three components were not as well aligned as with the fiber-optic system.

This causes the measured vorticity to be lower with the hybrid system. It also causes some lumpiness in the plots of V_θ , as shown in Fig. 38, and some differences in the core values of $V_{\theta c}$, as shown in Fig. 39.

There does appear to be consistency in the hybrid vorticity measurements, however. Blade-to-blade variations match well for both systems. Comparisons between different conditions measured with the hybrid system should therefore be valid, although the levels may be displaced.

Comparison of Velocity Measurements to Flow Models

Some comparisons of the measured results to flow models are useful to verify measured results and validate aspects of flow modeling. Calculations of Propeller 5168 performance in uniform inflow were made with the potential based panel method, PSF10¹. The method calculates the blade pressure distribution, spanwise loading, and overall propeller thrust and torque. From the measured circumferential-average tangential velocity, the blade spanwise circulation can be derived². Fig. 40 compares the measured circulation at the $x/R = 0.2386$ plane and the calculated blade circulation. Over the mid-span region, the measured and calculated results match closely. Near the tip, a significant deviation occurs due to the vortex formation and contraction. At the lowest loading condition of $J = 1.52$, negative circulation is seen, which corresponds to a weak secondary vortex, which is shown in the cross-plane plots in Fig. 27.

From the measured result, the pitch of the wake can be determined and compared to the wake model used in PSF10. The measured wake pitch is determined from:

$$P/D = \pi (r/R) (V_x)/(V_t) \quad (14)$$

The pitch of the blade wake is determined by averaging the flow pitch on either side of the blade viscous wake. This is compared to the geometric pitch and the pitch used in the PSF10 calculation, which is based on the model in the lifting surface code, PSF2³. Fig. 41 shows that there is a reasonable comparison over the midspan of the blade with the lifting surface model. The geometric pitch clearly underestimates the measured result. Also shown is the pitch of the vortex core, which was determined by tracking the noncavitating vortex core at the three near propeller downstream planes. It should be noted that the ultimate wake tip-vortex pitch derived using PSF2 has a value of 1.42, which compares well with the value shown of 1.43. Unfortunately, there is a discrepancy with the visually sighted cavitating tip-vortex pitch shown in Fig. 15, with a far wake value of 1.48, and near wake values as high as 1.6.

CONCLUSIONS

The work here presents perhaps the most detailed published measurements of a propeller tip vortex to date. All velocity components have been resolved in the rotating frame of the propeller with sufficient spatial resolution to reveal many details of the tip-vortex flow. These measurements were made at four different

advance coefficients and, at the primary advance coefficient of 1.10, at four different downstream planes. In addition, the full Reynolds-stress tensor was measured in one plane for the primary advance coefficient. These measurements will be useful not only as a numerical test case, but also as a guide to better understanding the physics of tip-vortex flows.

The measurements were performed with two different LDV systems. The hybrid LDV system measured only the mean velocities and the normal stresses. The fiber-optic system measured the shear stresses as well. The uncertainty analysis shows that, for most of the flow, the both systems measure the flowfield with excellent accuracy. However, very near the tip vortex, the high turbulence intensities and high velocity gradients reveal certain limitations of the hybrid system. The inability to precisely align the three measurement volumes in the hybrid system makes the measurements of lower accuracy in the tip-vortex region. This is reflected most in the measurements of streamwise vorticity; the hybrid system measurements of ω_s are consistently lower than the measurements made with the fiber-optic system.

Although every attempt was made to match the measurements made with the fiber-optic LDV system to those made with the hybrid system, the two sets were made at slightly different flow conditions. It appears that the window insert used with the hybrid system caused a small flow asymmetry which made matching the flow conditions impossible.

Strong asymmetry in the tip vortex was observed due to interaction with the wake. This asymmetry decreased as the flow moved downstream and the vortex separated from the wake.

Vortex strength varied strongly with advance coefficient. Though quite distinct at $J = 0.98$ and 1.10 , the tip vortex was very weak at the design J of 1.27 , and at $J = 1.52$, the tip vortex was virtually non-existent. In cavitation inception tests, no tip cavitation was observed at the two highest advance coefficients.

Small but significant differences were observed in vortex strength and position from blade to blade. The blade-to-blade variation was consistent with both LDV systems. Any comparisons of this data to calculations of the tip vortex should take into account this variation. Vortex cores should be aligned before making direct comparisons, and calculated quantities should be compared to the range of measurements.

REFERENCES

1. Kerwin, J.E., et. al., "A Surface Panel Method for the Hydrodynamic Analysis of Ducted Propellers," *Transactions SNAME*, Vol. 95, 1987.
2. Kerwin, J.E., "Flow Field Computations for Non-cavitating and Cavitating Propellers," *14th Symposium on Naval Hydrodynamics*, Ann Arbor, Michigan, 1983.
3. Greeley, D.S. and Kerwin, J.E., "Numerical Methods for Propeller Design and Analysis in Steady Flow," *Transactions SNAME*, Vol. 90, 1982.

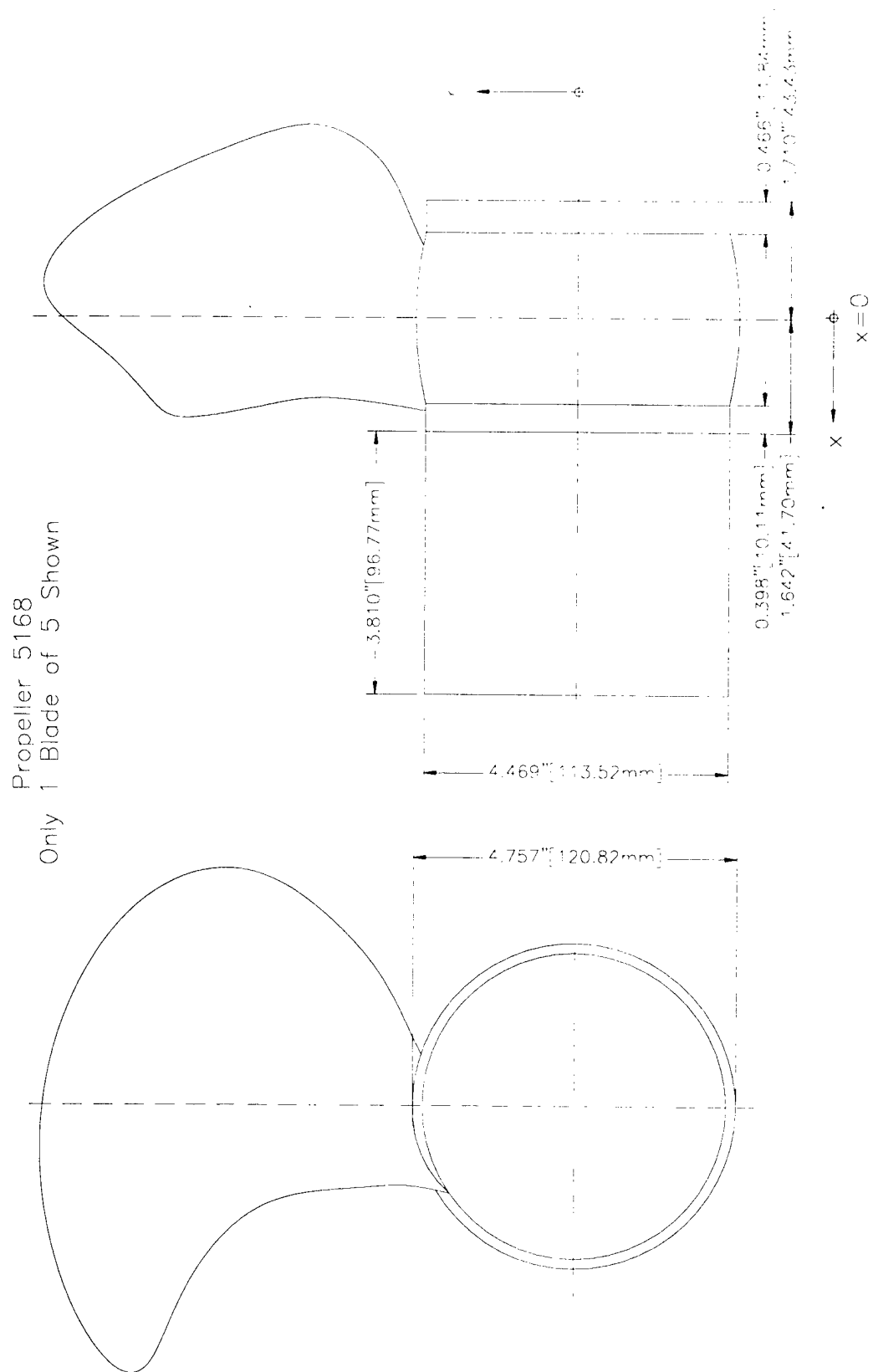


Fig. 1. Propeller 5168, with fairwater.

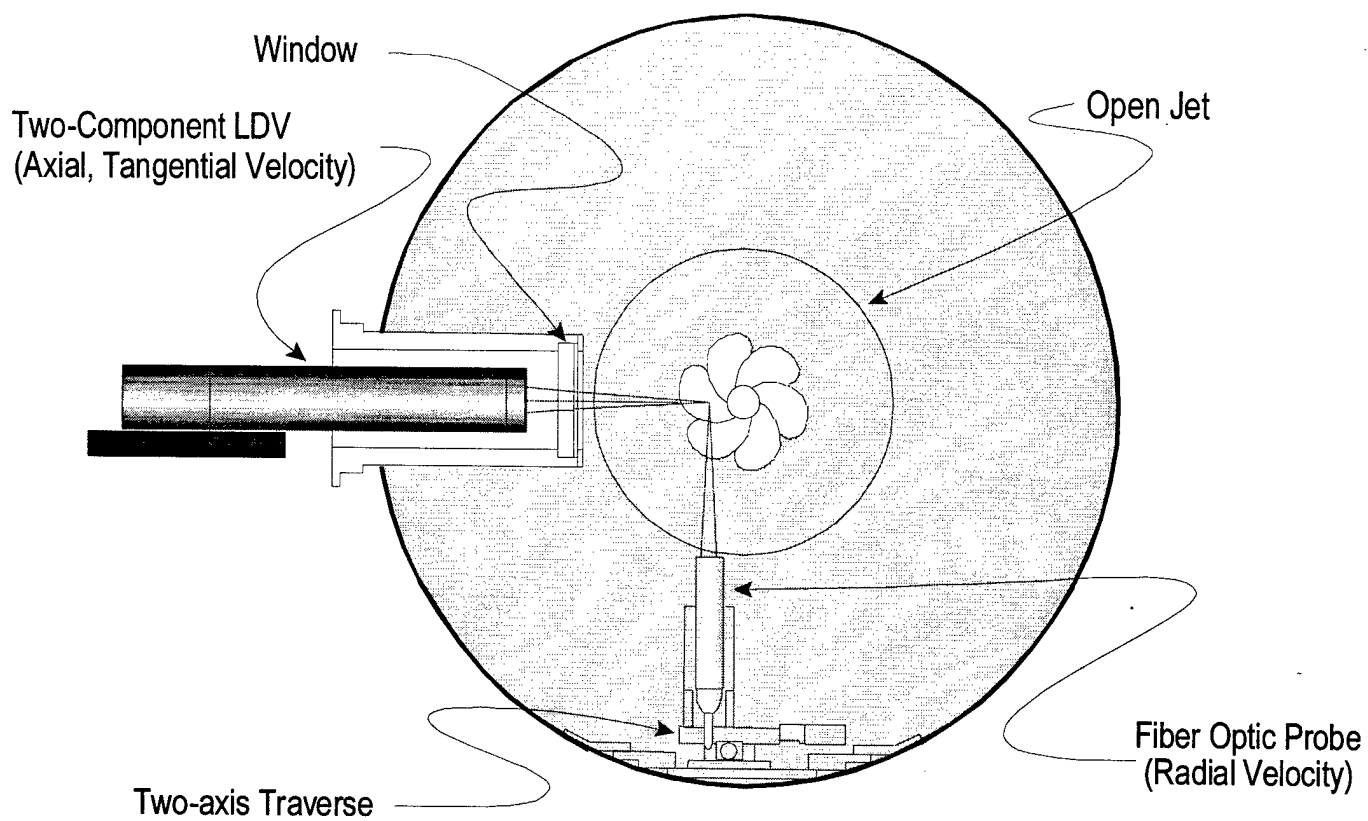


Fig. 2 Hybrid lens-optic/fiber-optic LDV system in the 36-inch water tunnel.

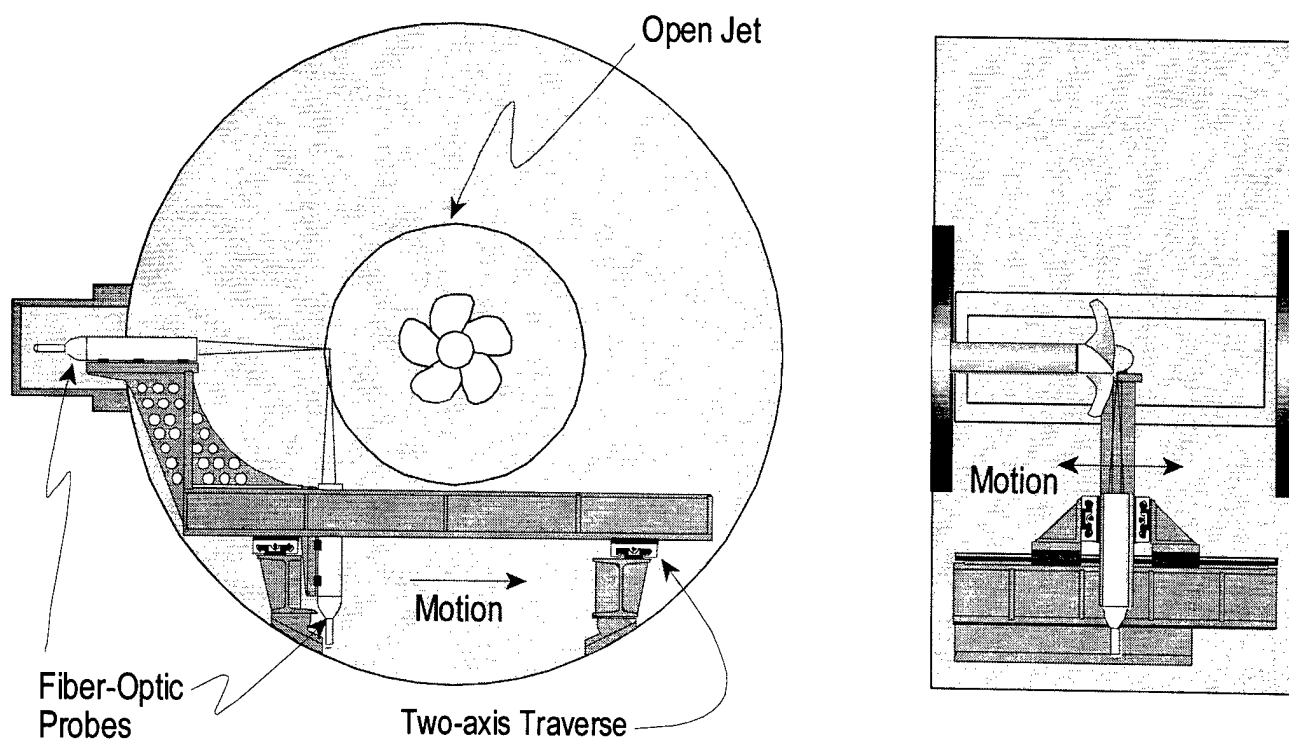


Fig. 3 All fiber-optic LDV system in the 36-inch water tunnel.

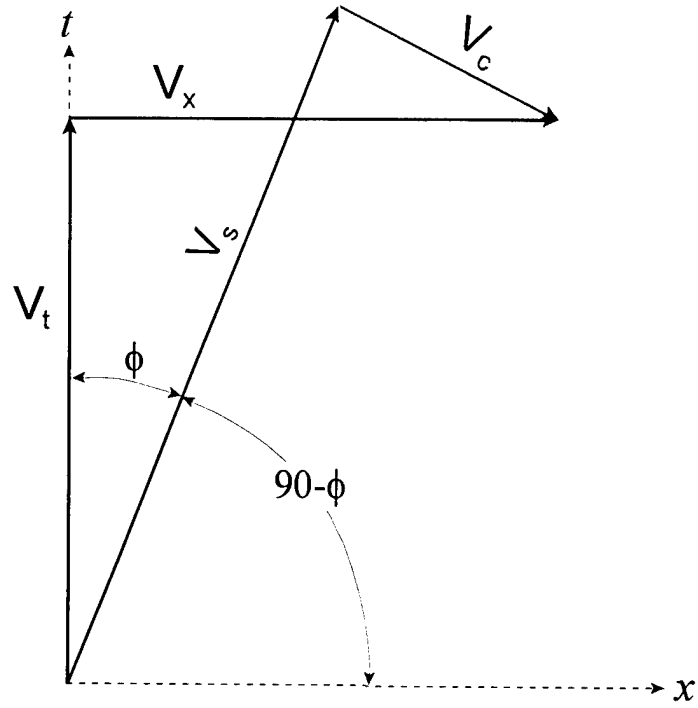


Fig. 4. The secondary-flow coordinate system.

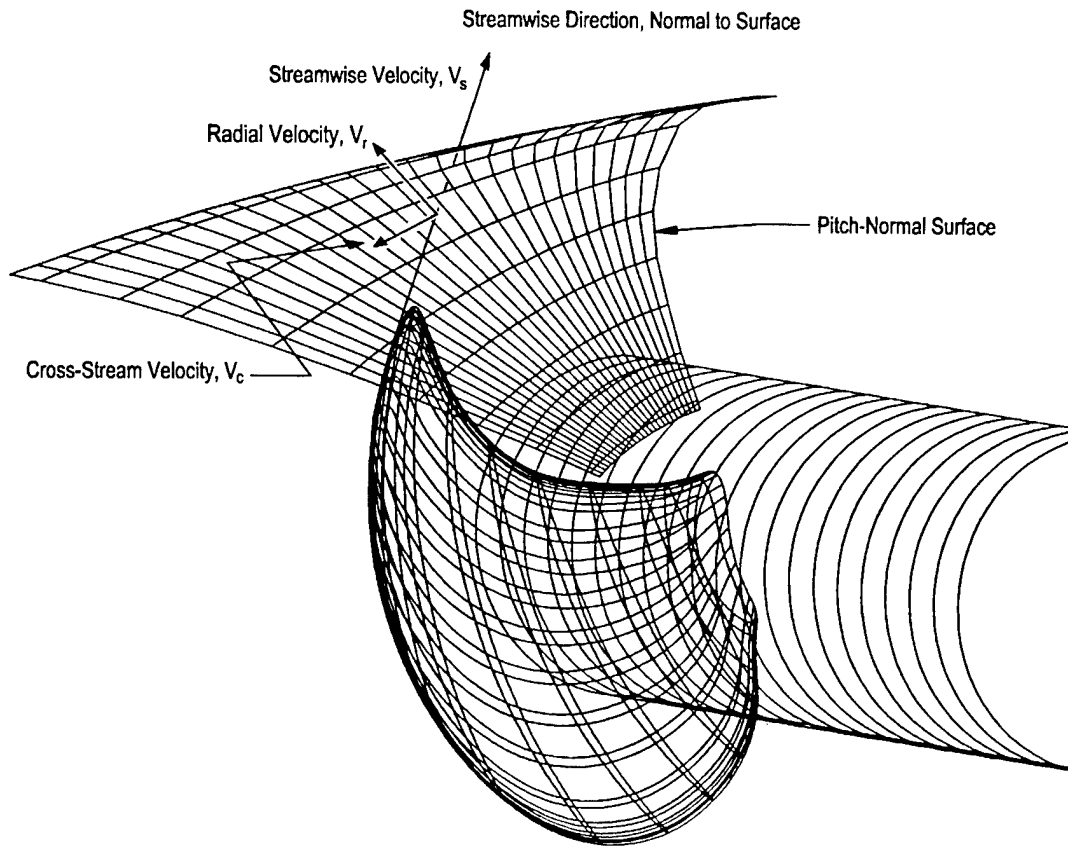


Fig. 5. Pitch-line perpendicular plane for secondary flow presentation.

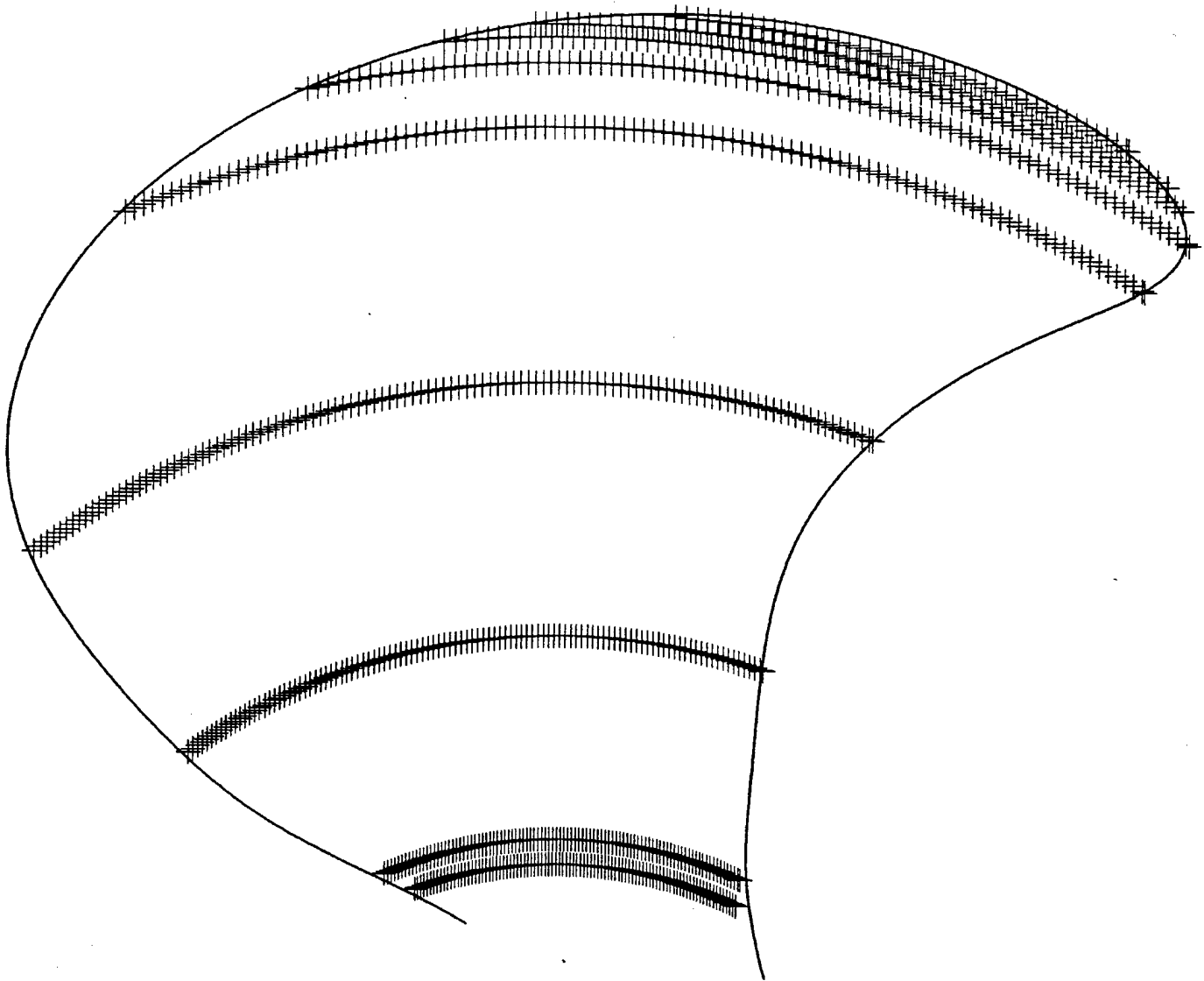


Fig. 6. Propeller 5168 blade measurement matrix.

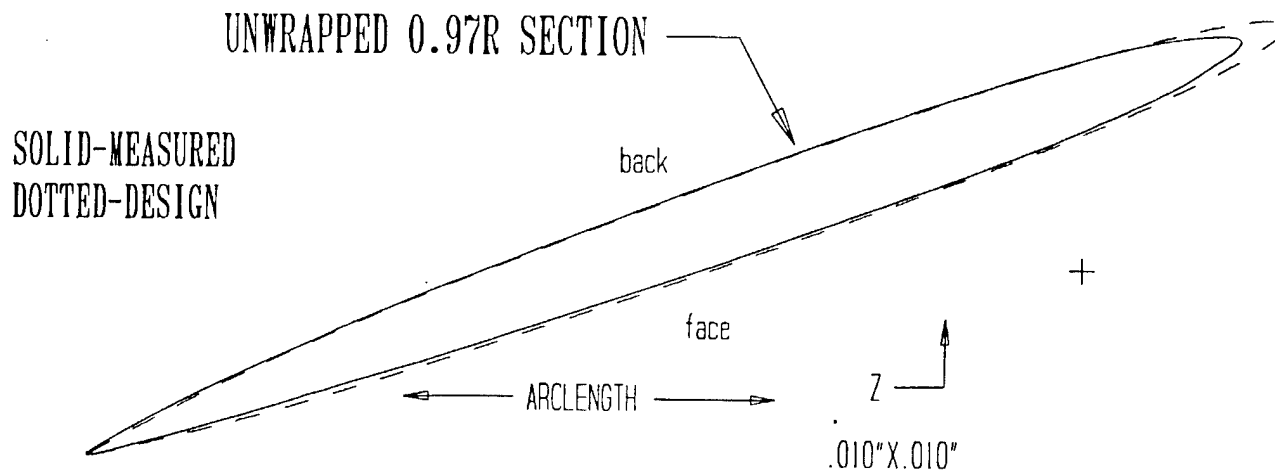


Fig. 7a. Typical cut back leading edge, $r = 0.97$.

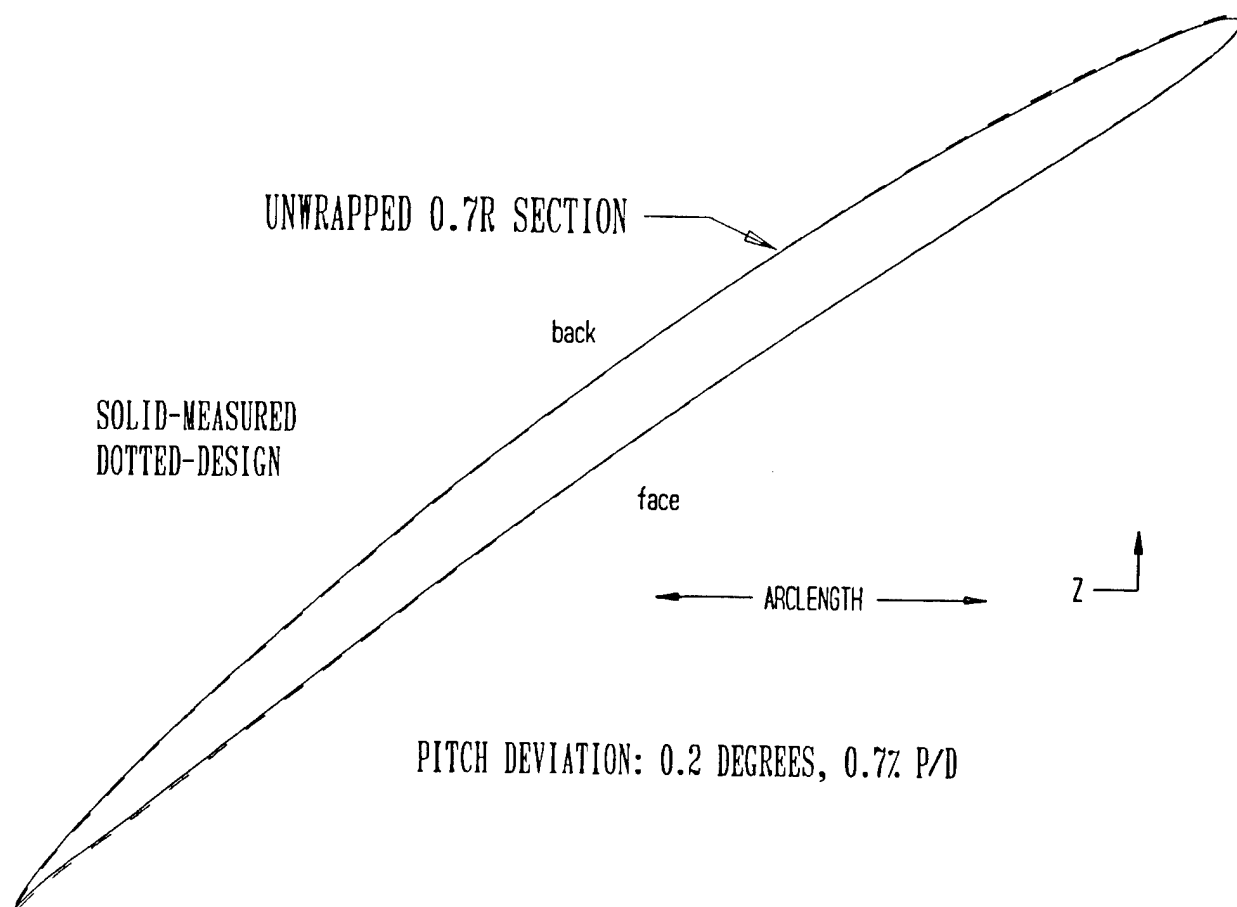


Fig. 7b. Typical good comparison, $r = 0.7$.

Fig. 7. Comparison of measured and design blade profiles.

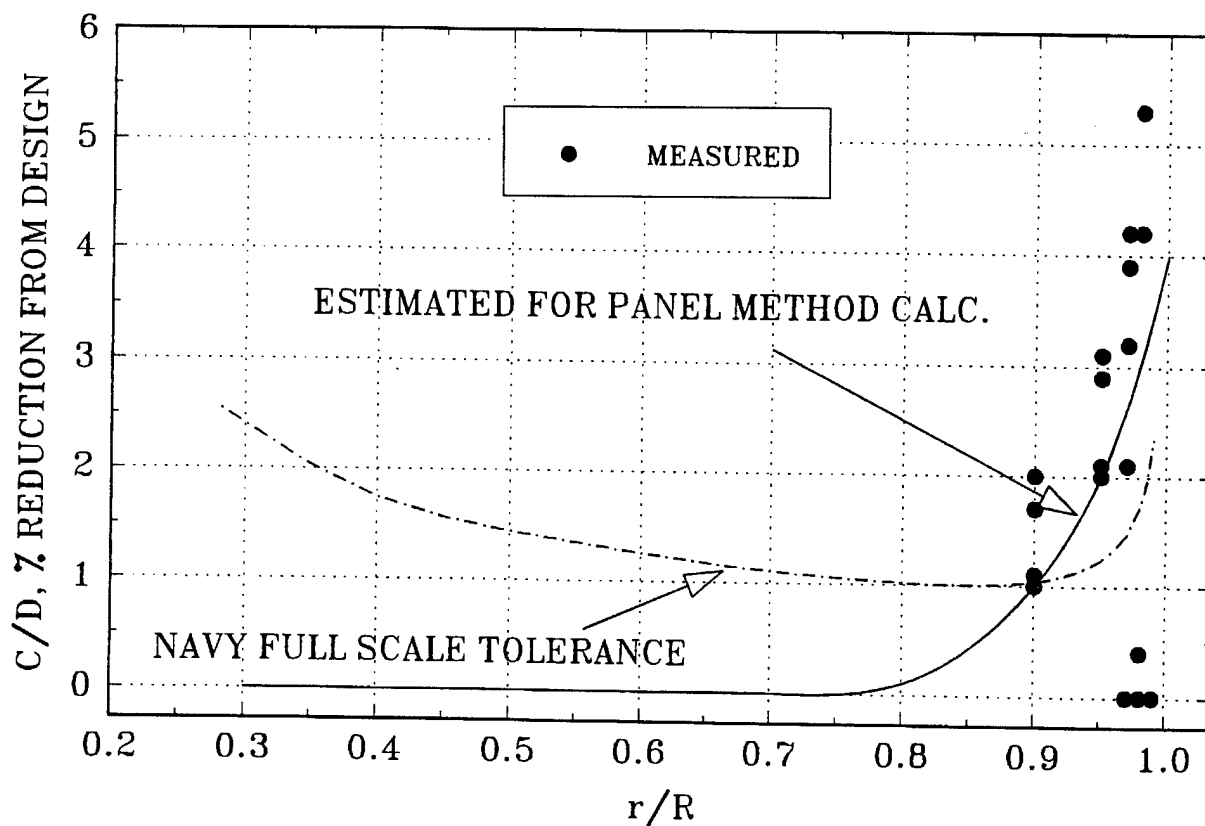


Fig. 8. Estimated chord-length cutback from measured section offsets.

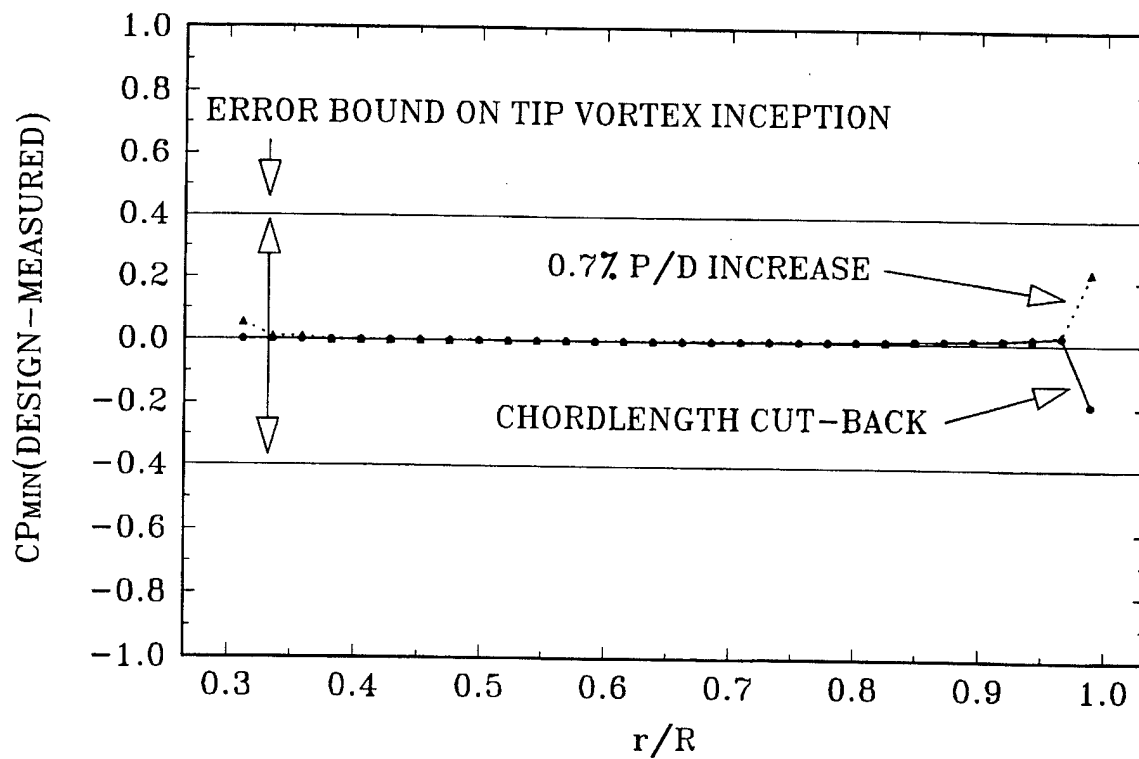


Fig. 9. Predicted minimum C_p variations due to geometry perturbations.

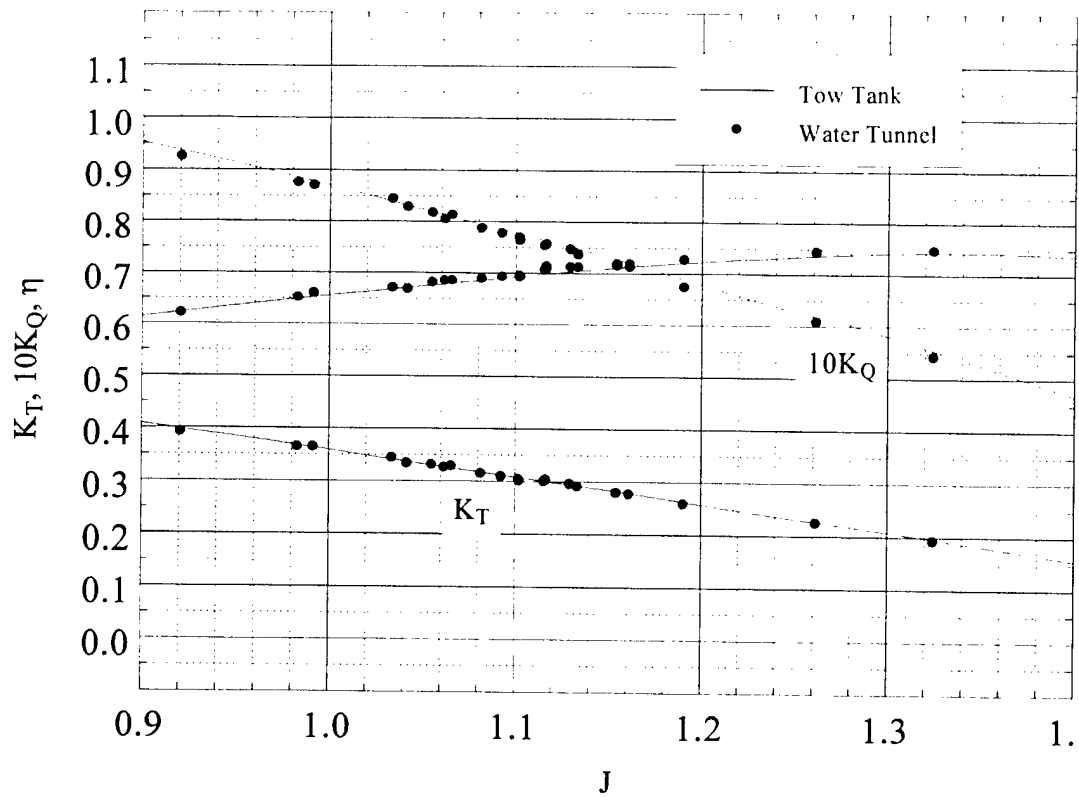


Fig. 10. Performance of propeller 5168.

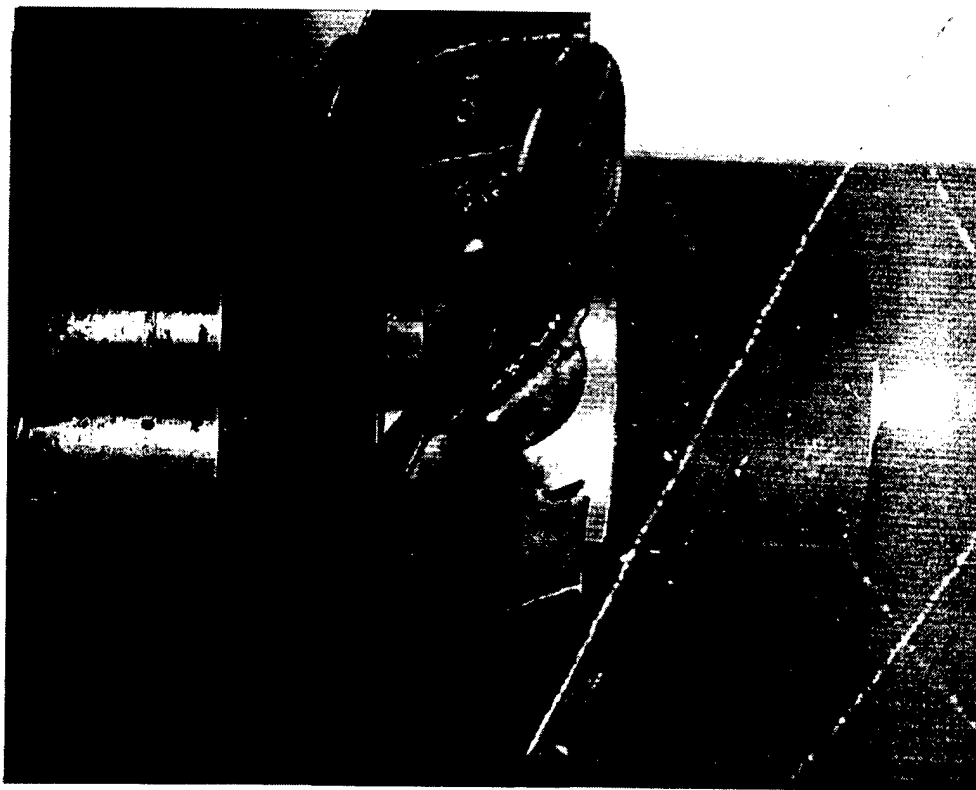


Fig. 11. Propeller 5168 with cavitating tip vortices.

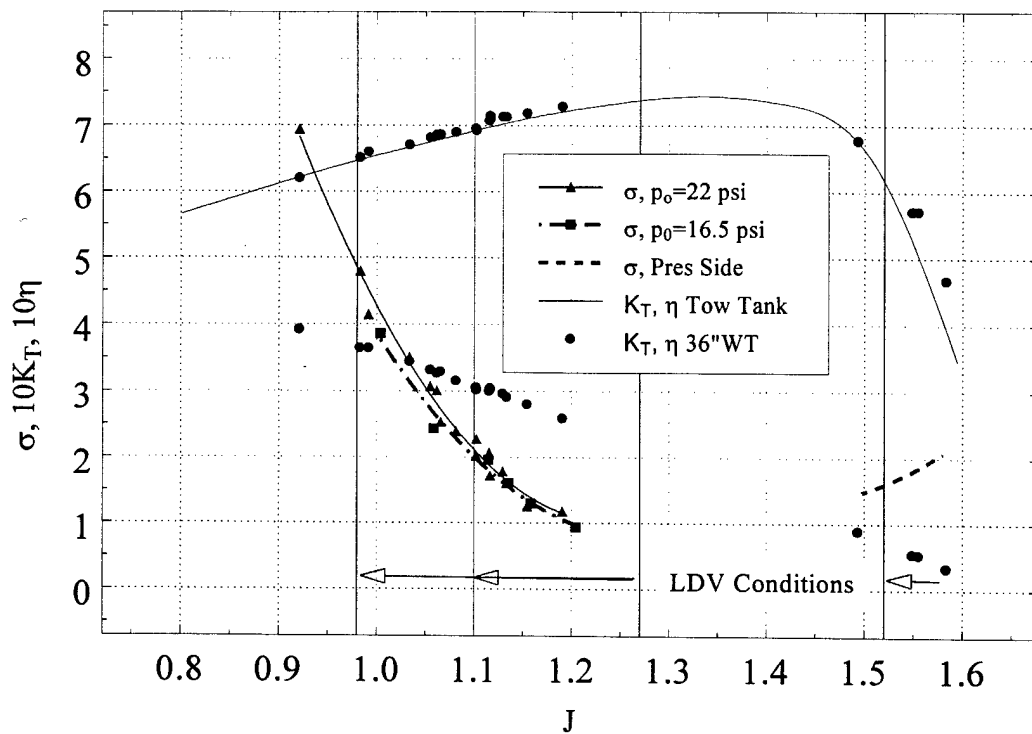


Fig. 12. Tip-vortex cavitation inception for propeller 5168 vs. J .

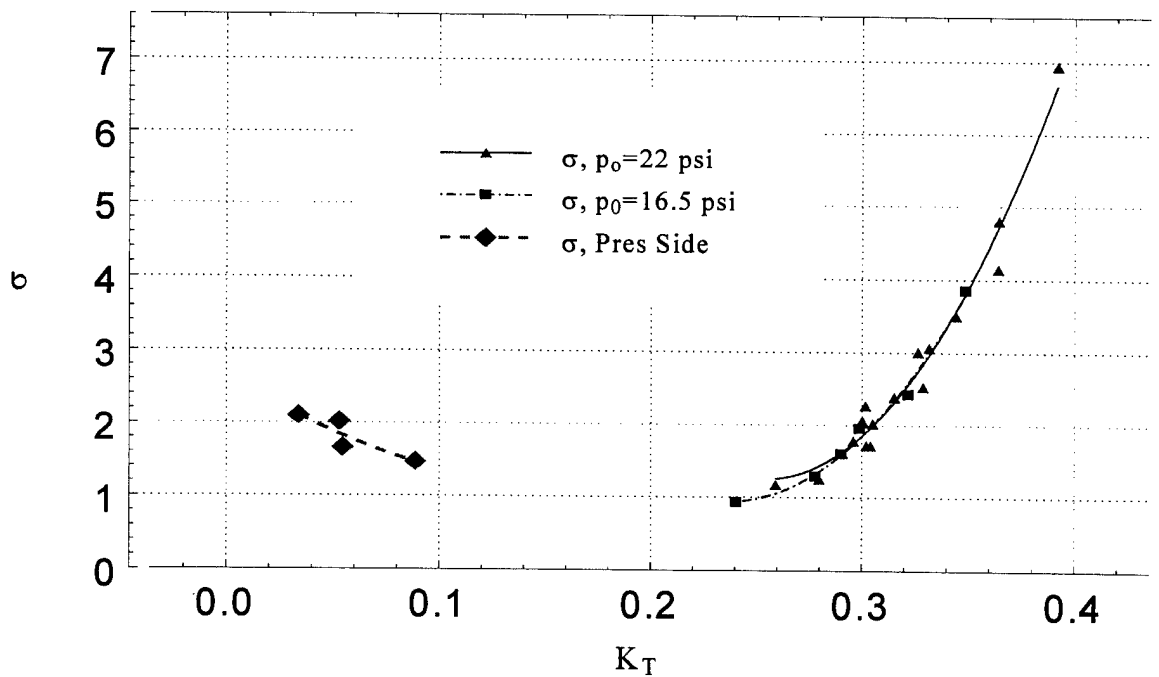


Fig. 13. Tip-vortex cavitation inception for propeller 5168 vs. K_T .

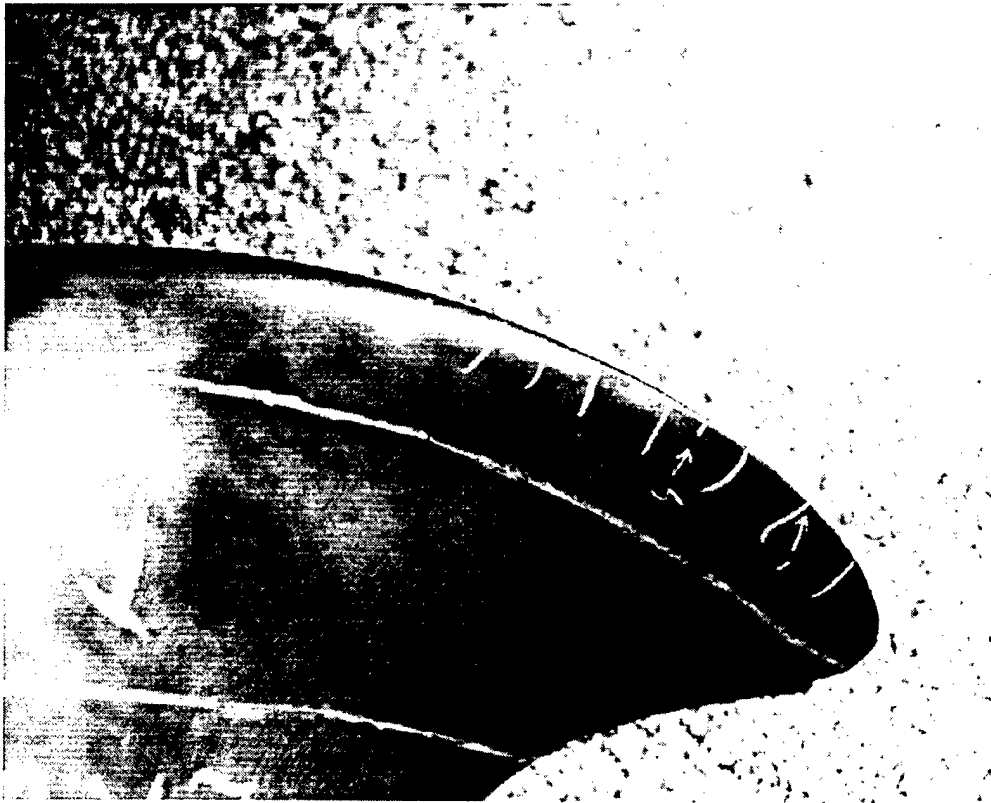


Fig. 14a. Attachment locations for blade1.

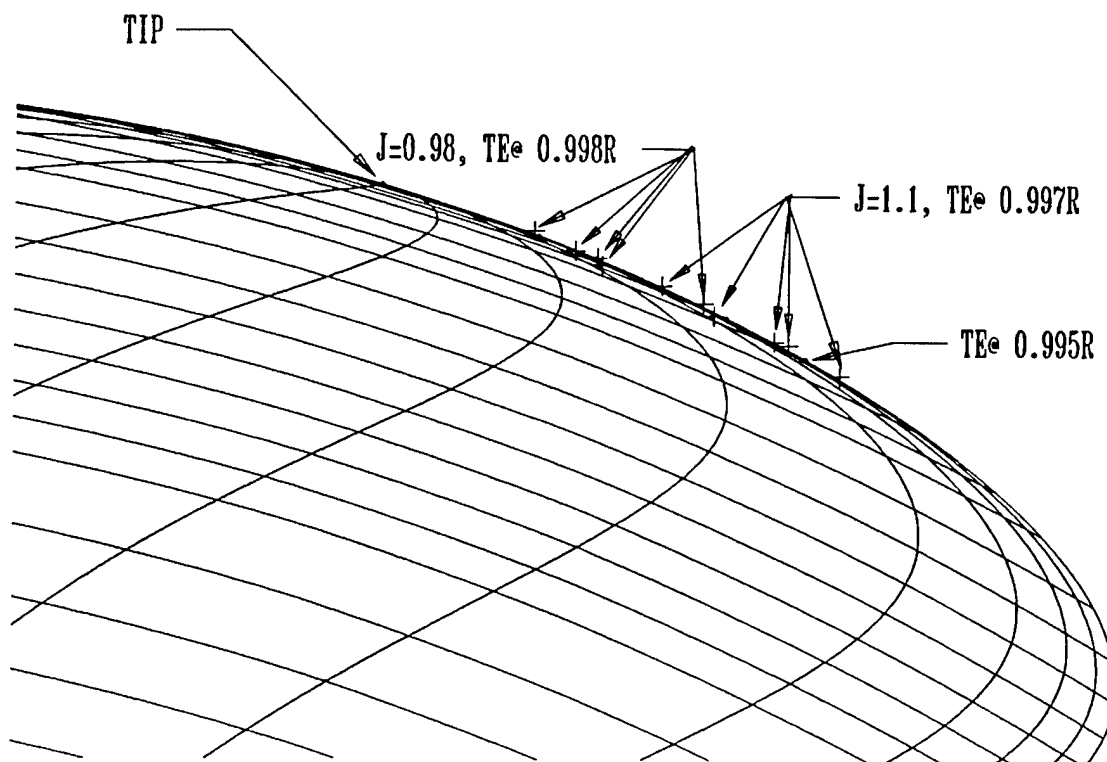


Fig. 14b. Attachment locations for all blades.

Fig. 14. Location of attached tip vortex at $J = 0.98$ and 1.10 .

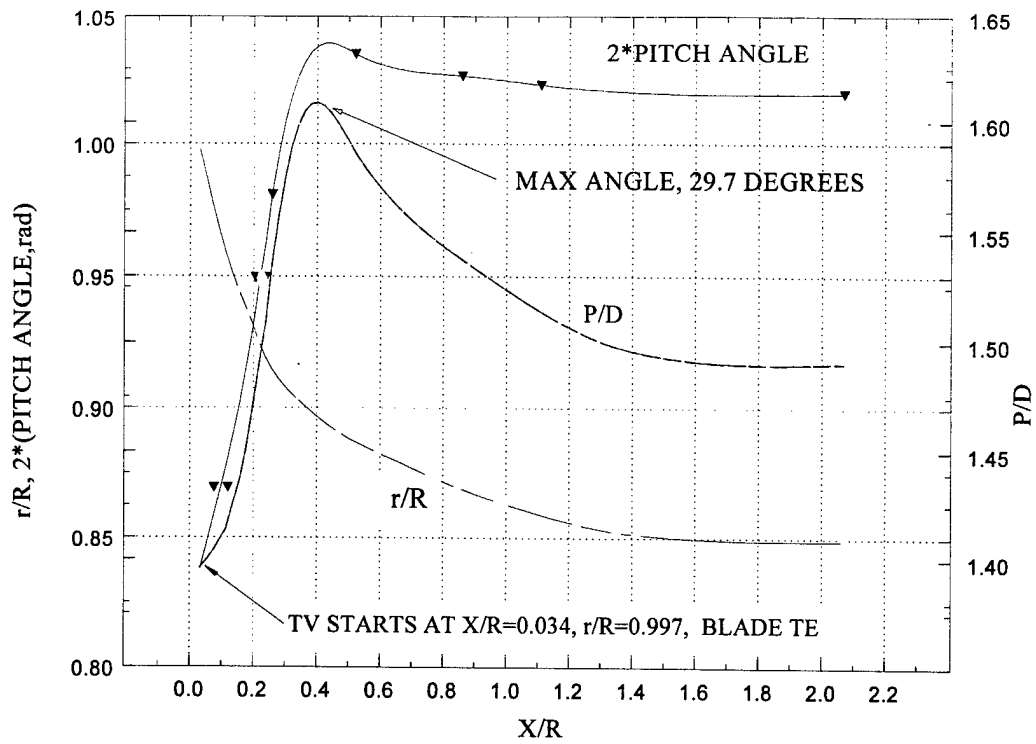


Fig. 15. Propeller 5168 tip-vortex trajectory.

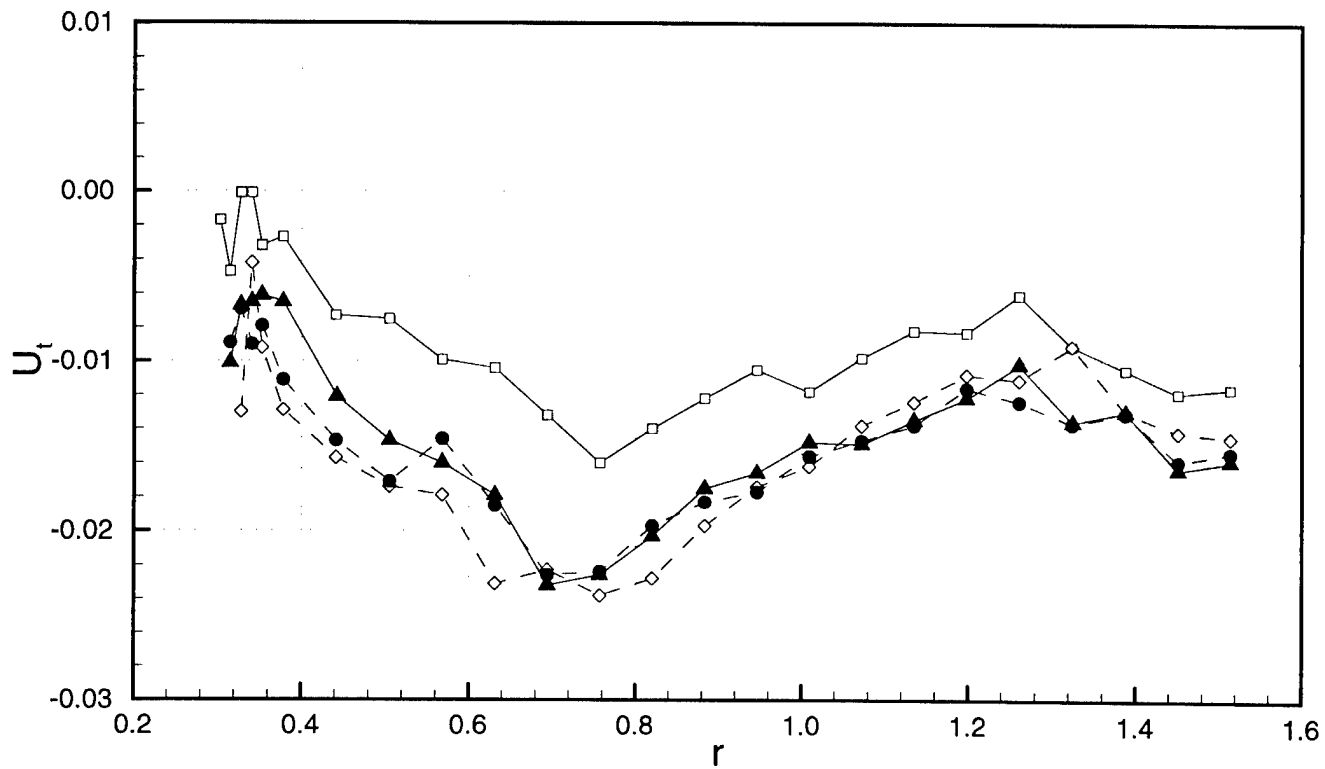
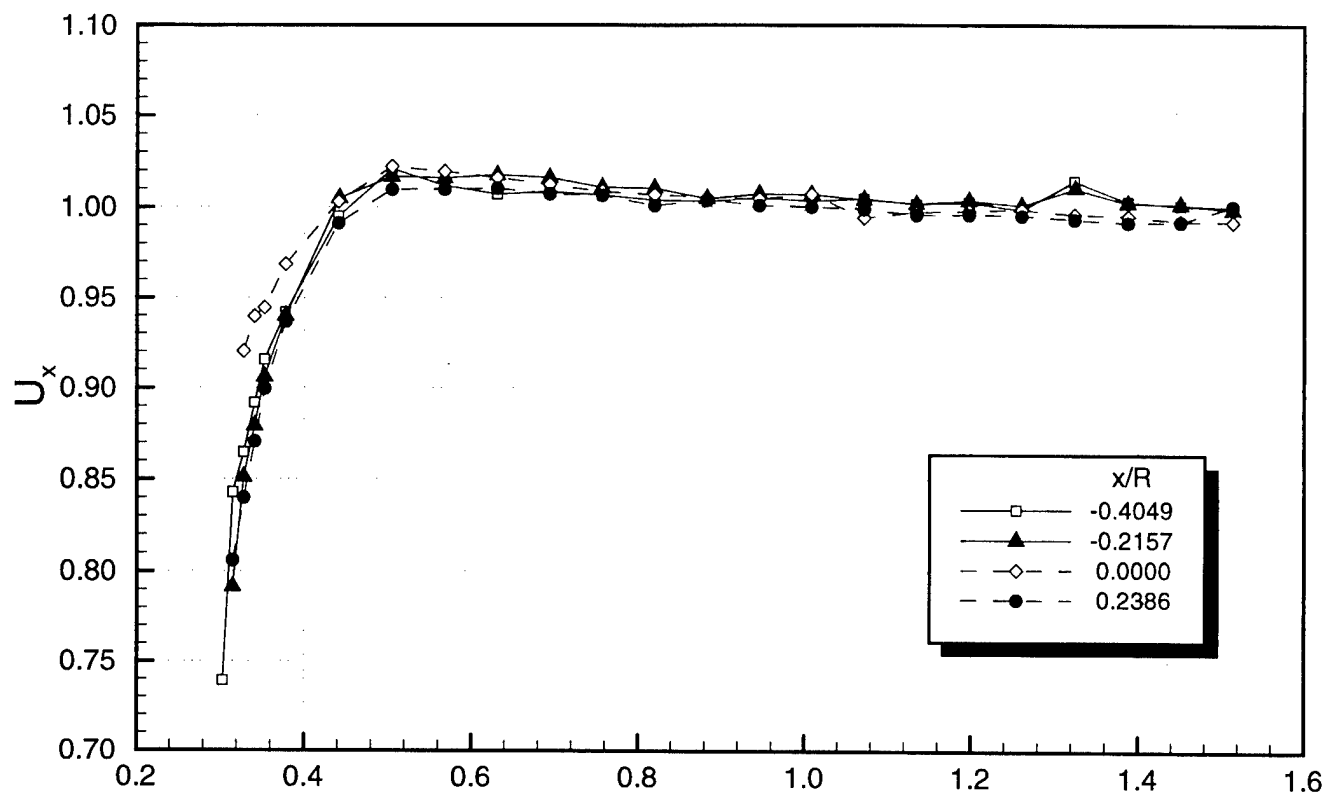


Fig. 16. Circumferentially averaged velocity with dummy hub.

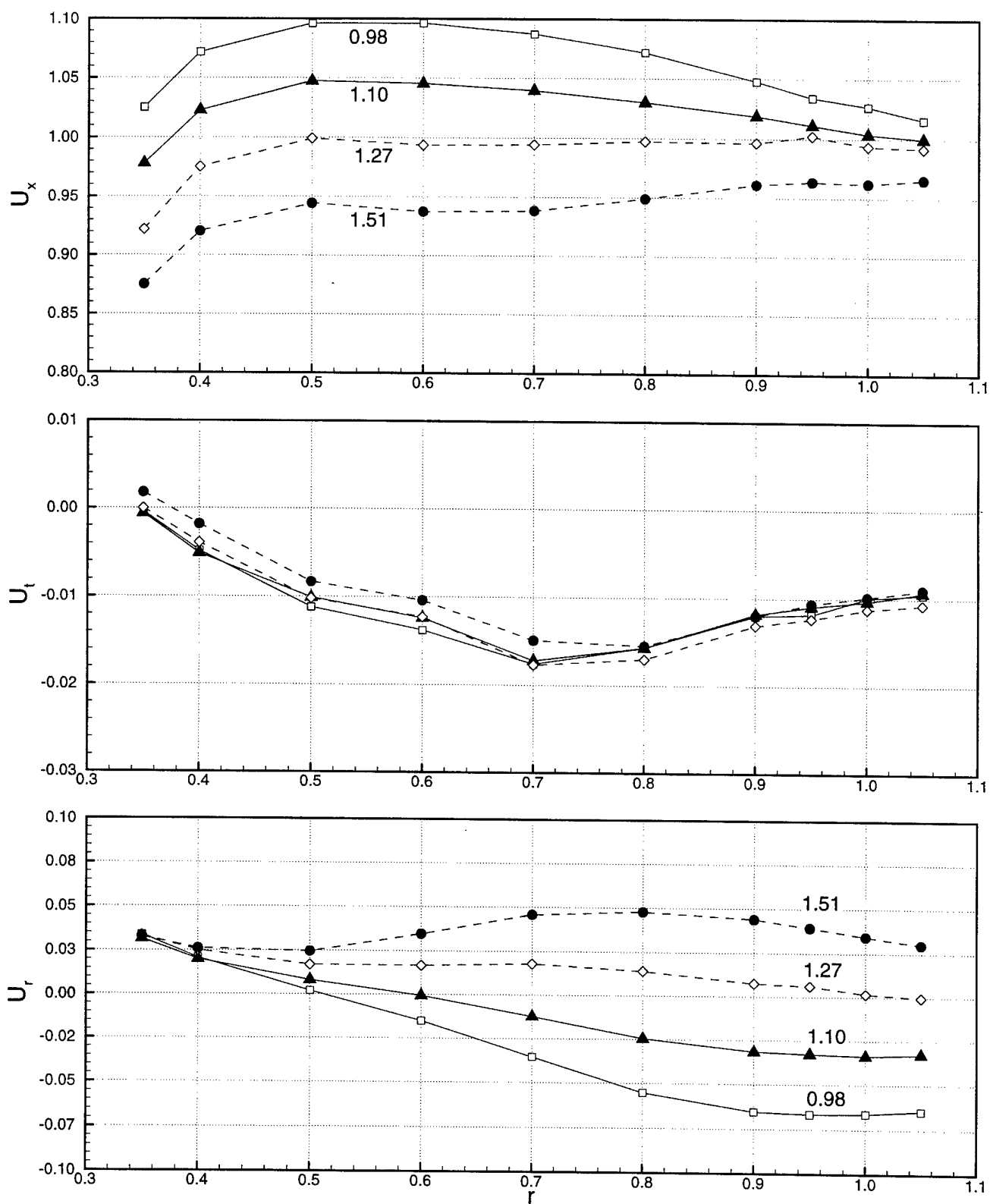


Fig. 17. Circumferentially averaged inflow velocity variation with J , $x/R = -0.4049$.

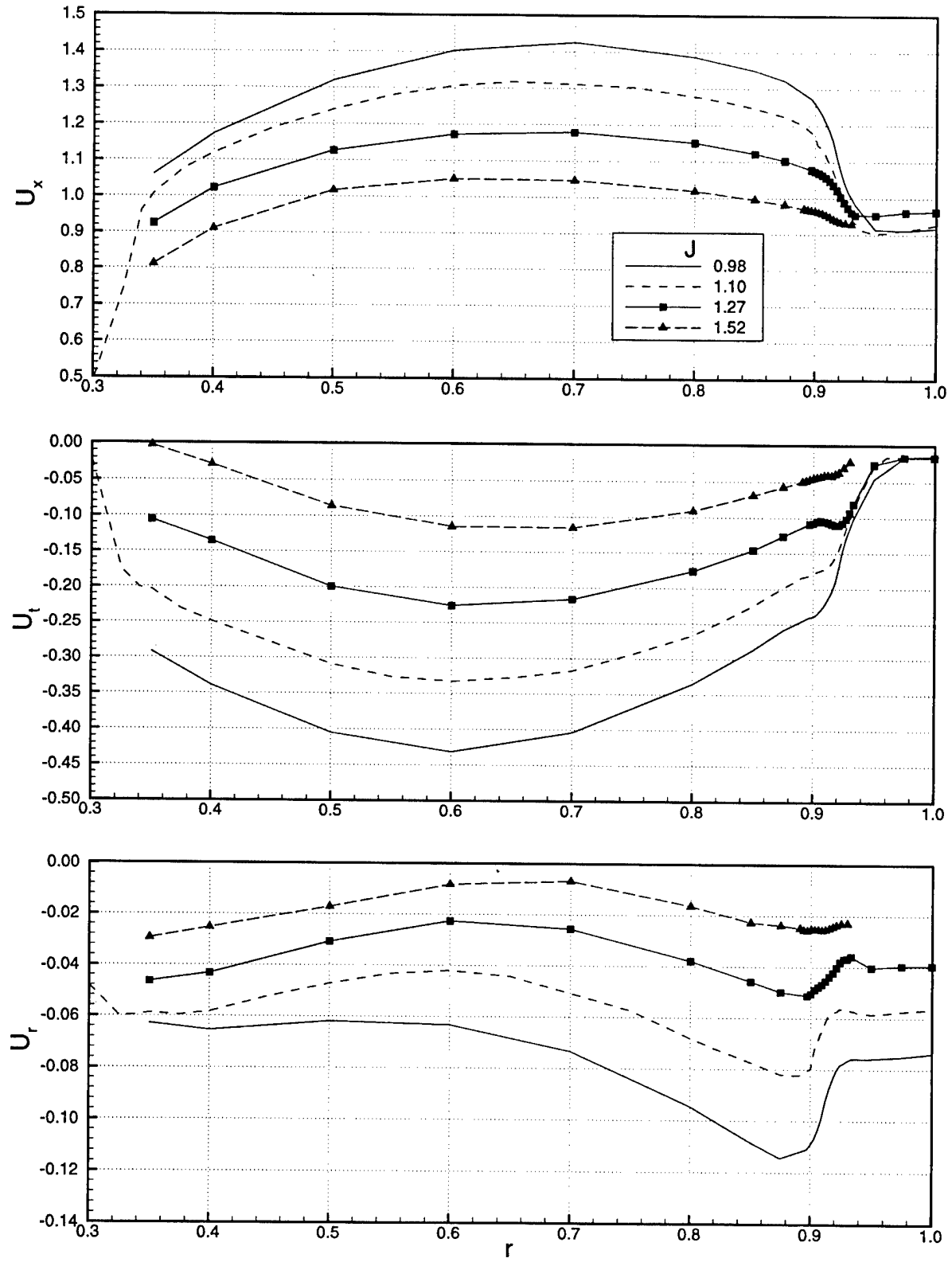


Fig. 18. Circumferentially averaged velocity variation with J , $x/R = 0.2386$.

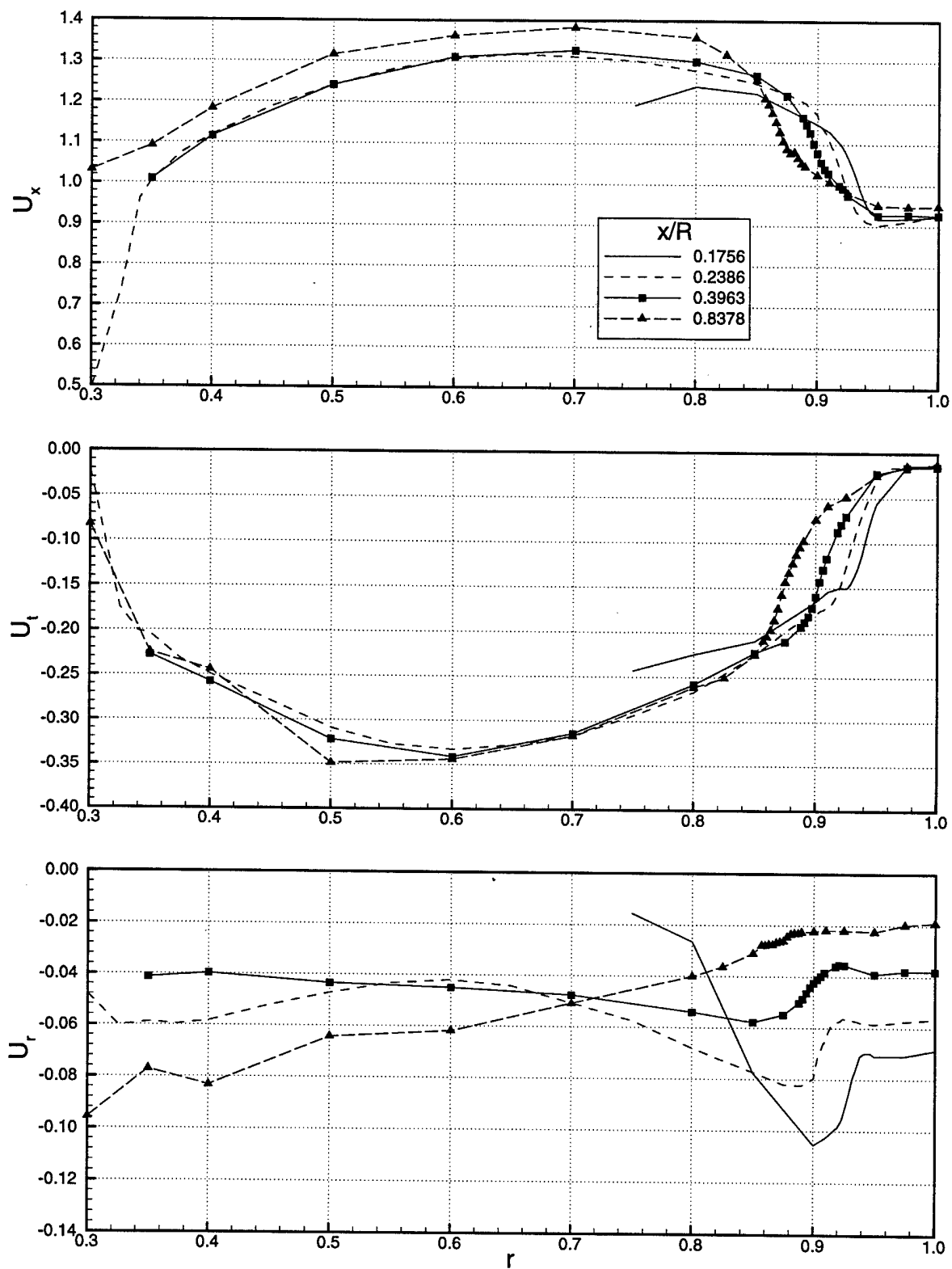


Fig. 19. Circumferentially averaged velocity variation with x , $J = 1.10$.

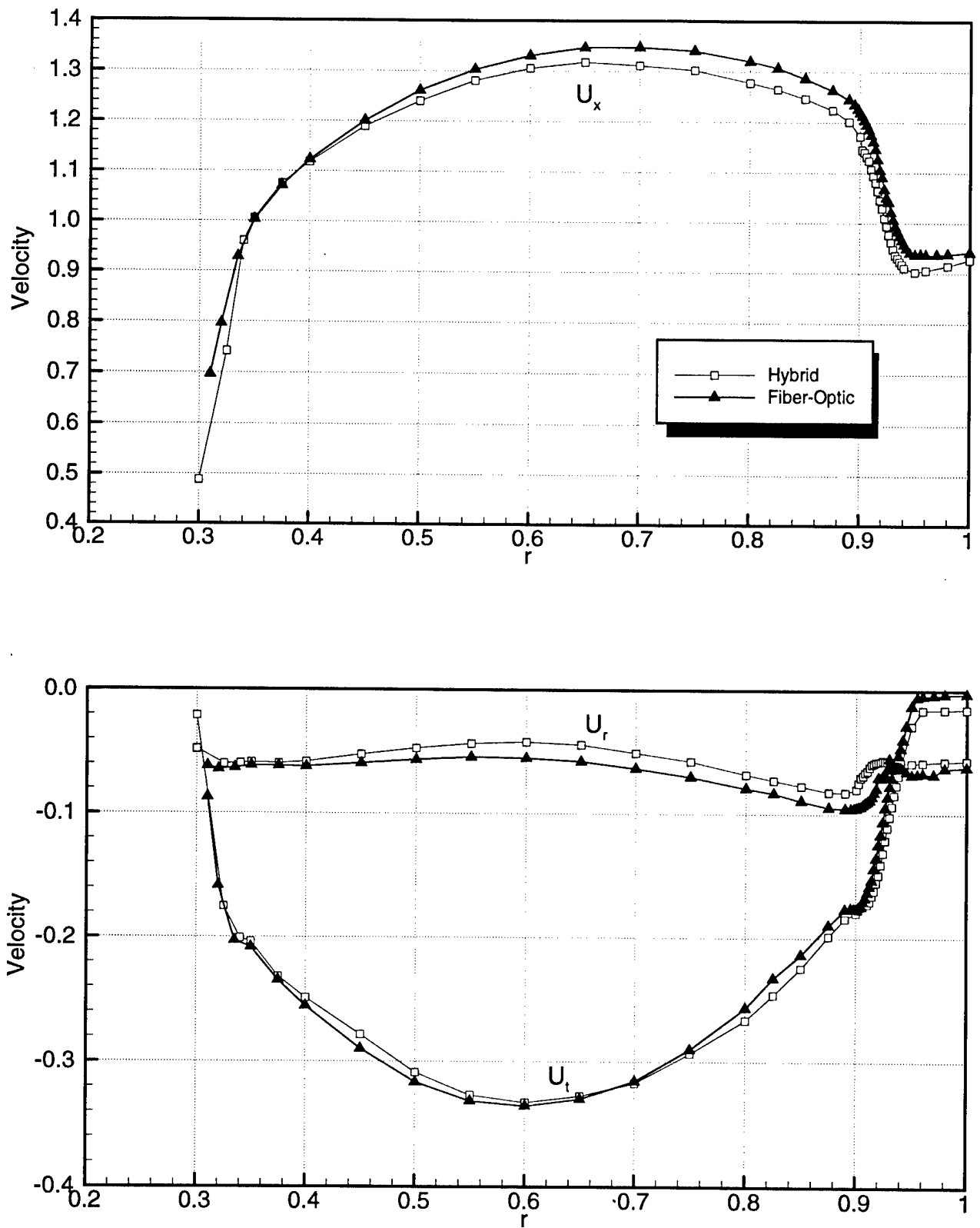


Fig. 20. Circumferentially averaged velocities, hybrid vs. fiber-optic data set, $J = 1.10$, $x/R = 0.2386$.

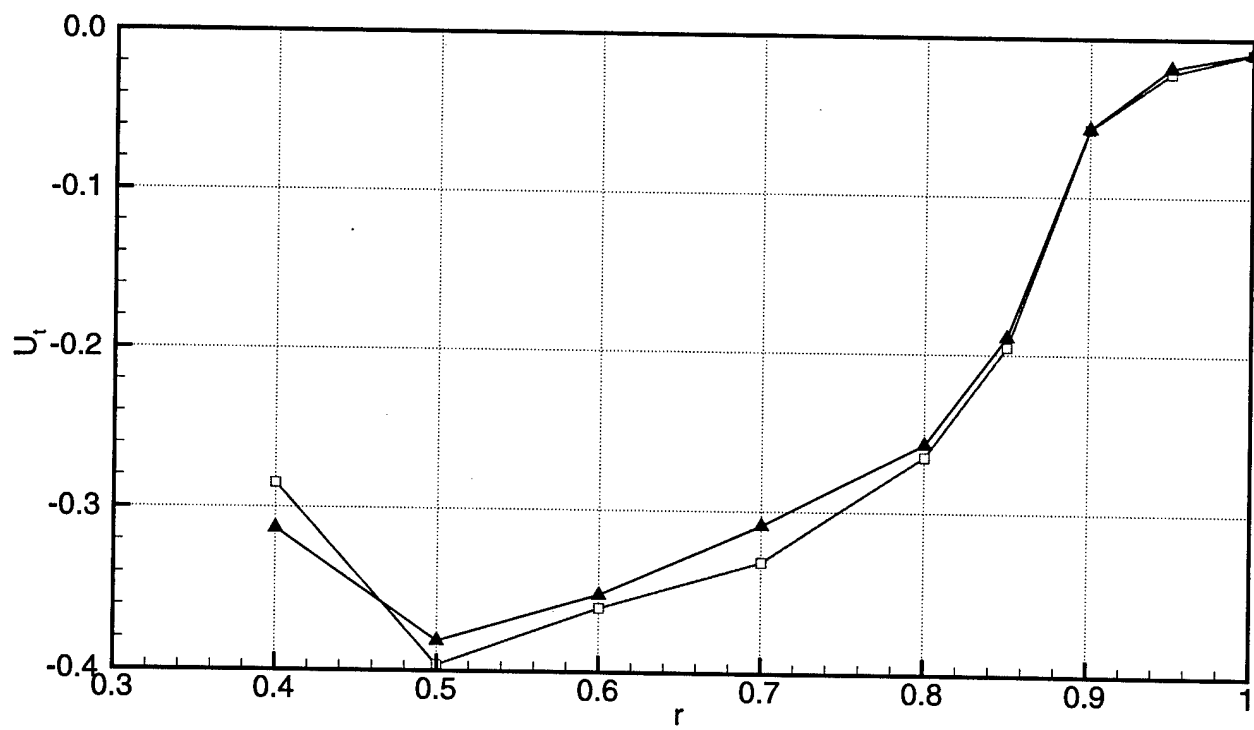
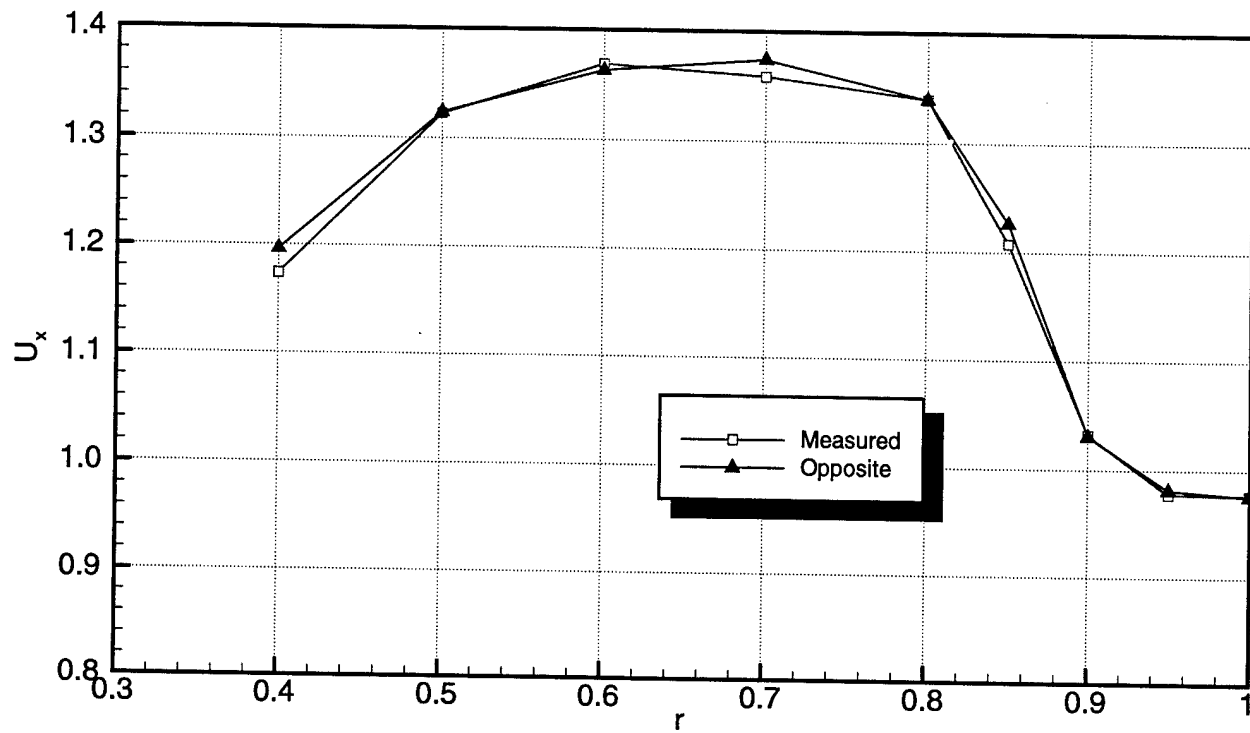


Fig. 21. Circumferentially averaged velocity asymmetry, hybrid data set, $J = 1.10$, $x/R = 1.091$.

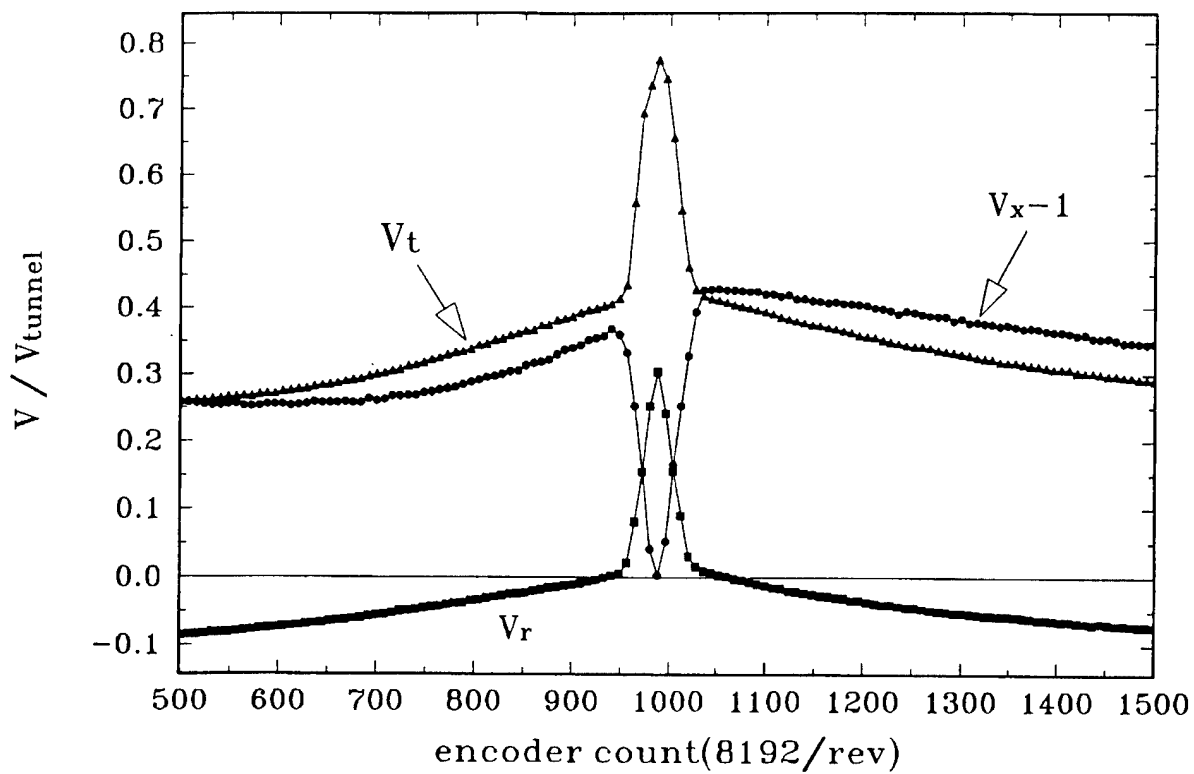


Fig. 22a. $r = 0.70$, $x/R = 0.2386$.

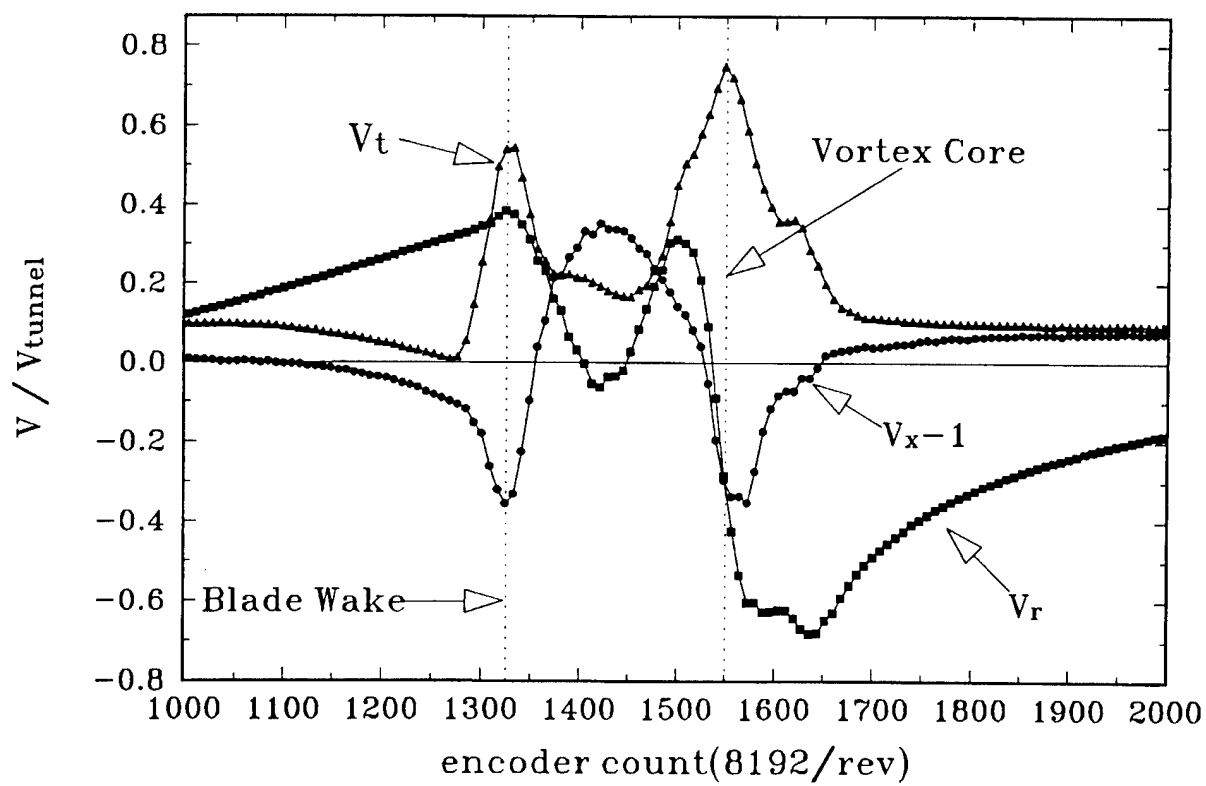


Fig. 22b. $r = 0.92$, $x/R = 0.2386$.

Fig. 22. Propeller wake velocities in the stationary frame.

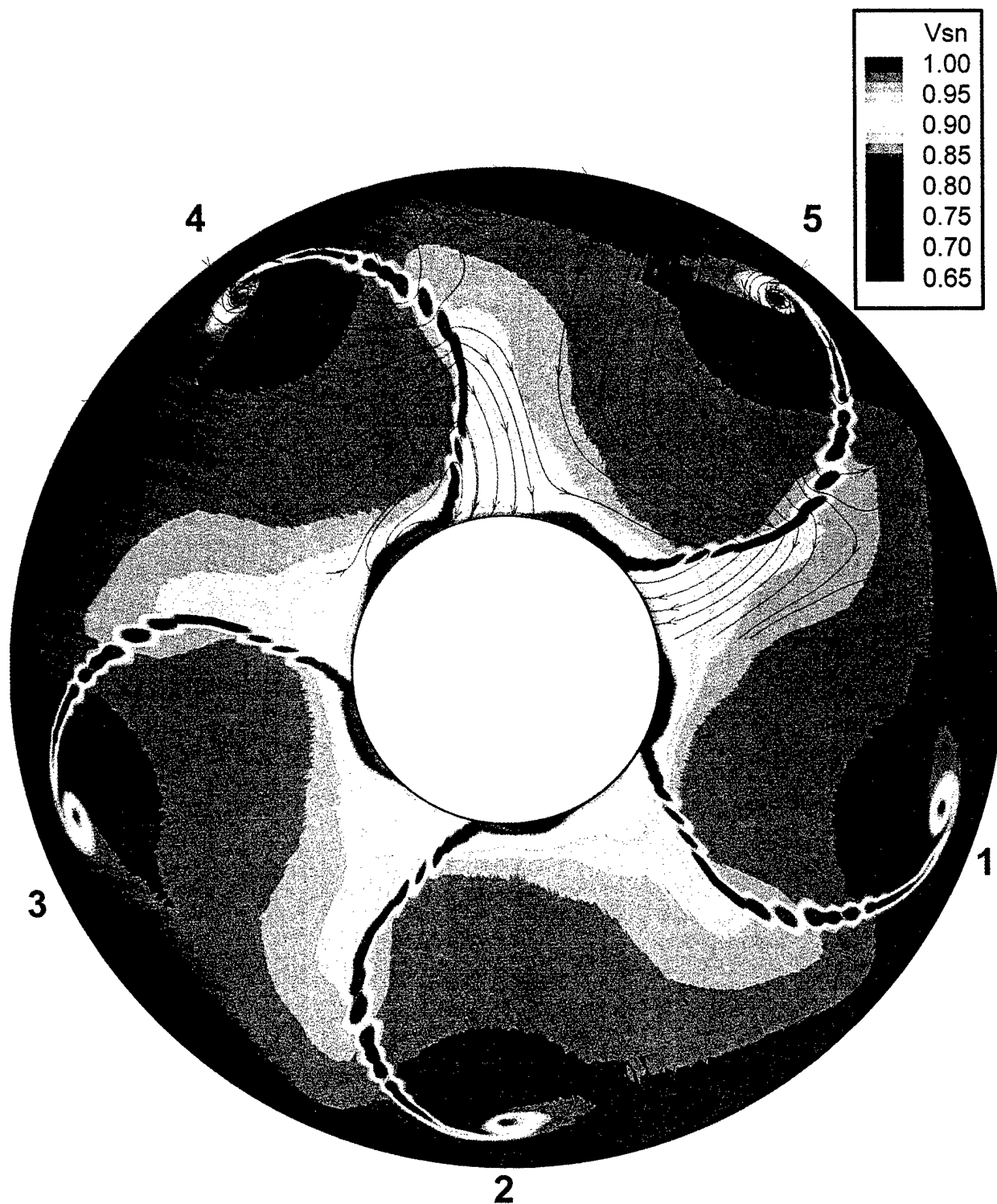


Fig. 23. Contours of the streamwise velocity, with secondary flow particle traces.

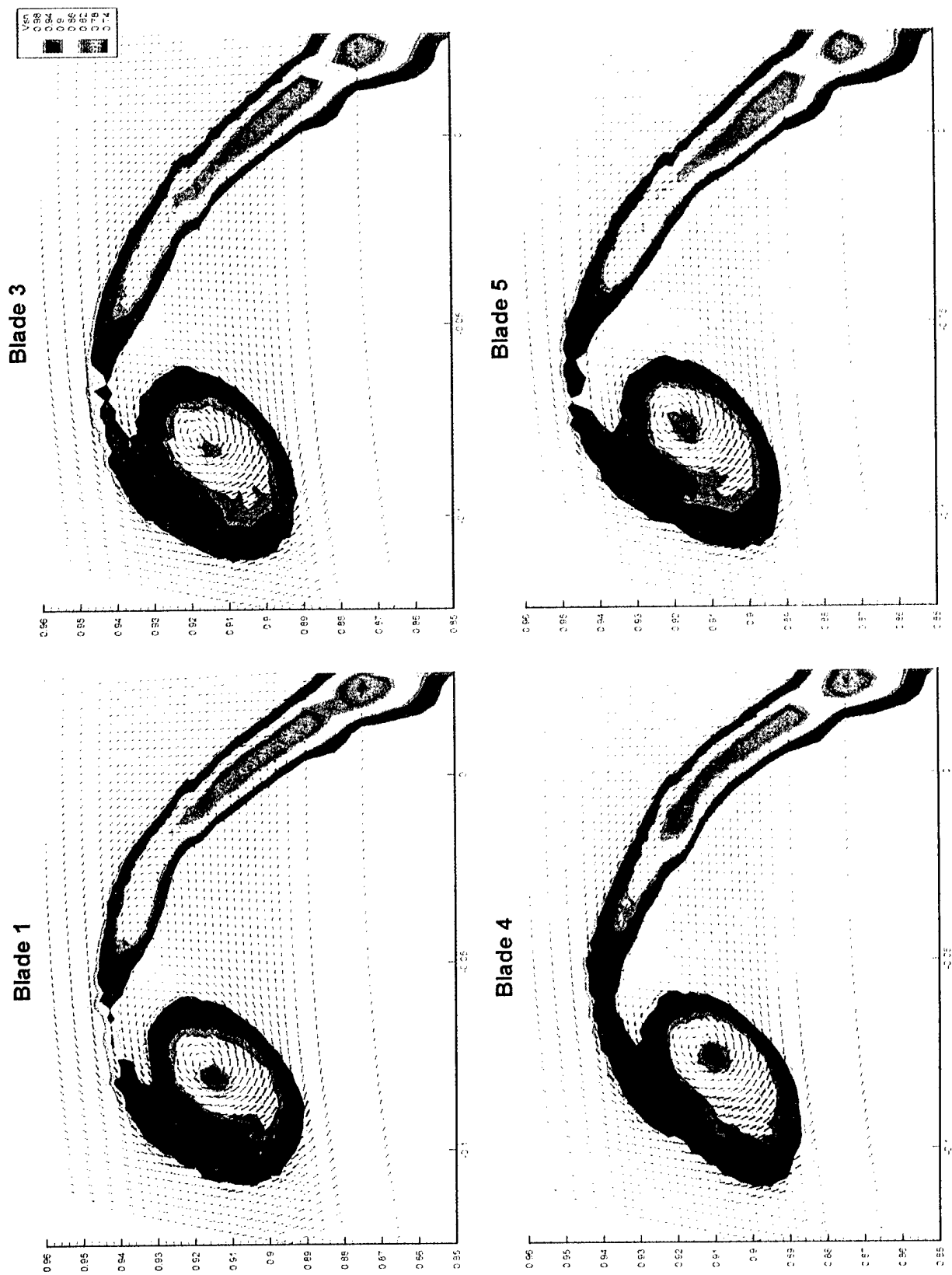


Fig. 24. Blade-to-blade variation of the tip vortex, contours of V_t/V_∞ with secondary flow vectors.

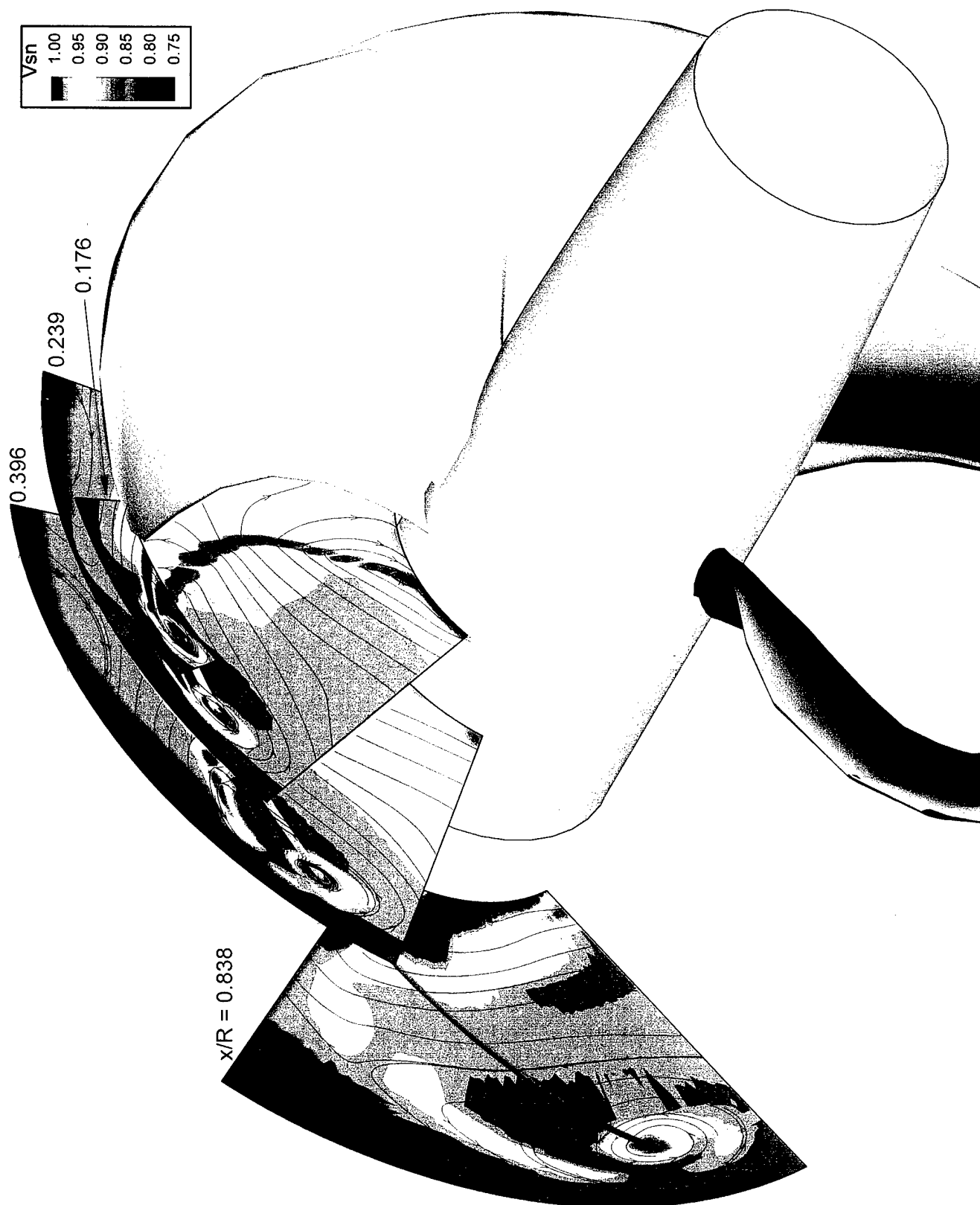


Fig. 25. Contours of V/V_{∞} downstream of the propeller, $J = 1.10$.

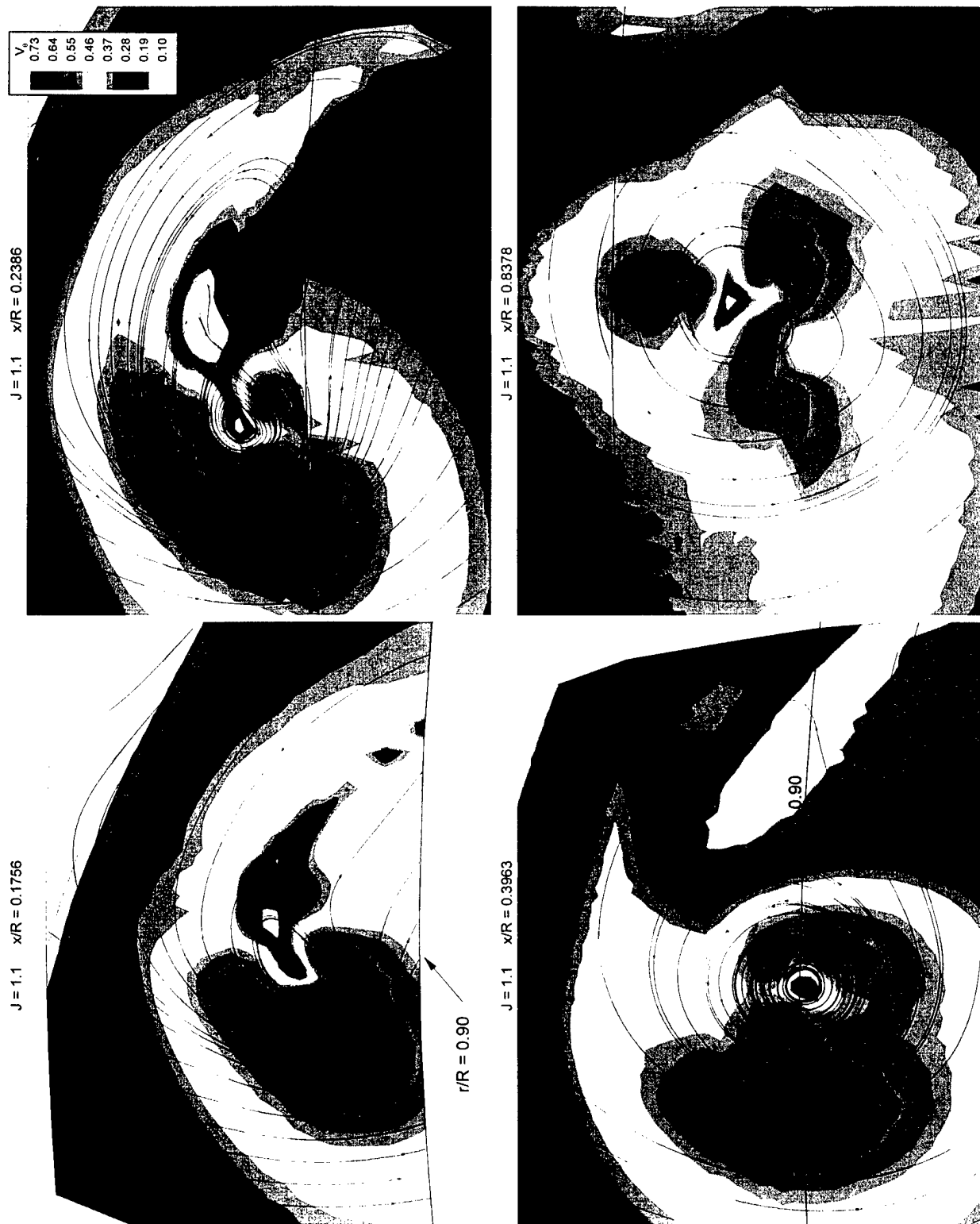


Fig. 26. Development of the tip-vortex flow, moving downstream, $J = 1.10$.

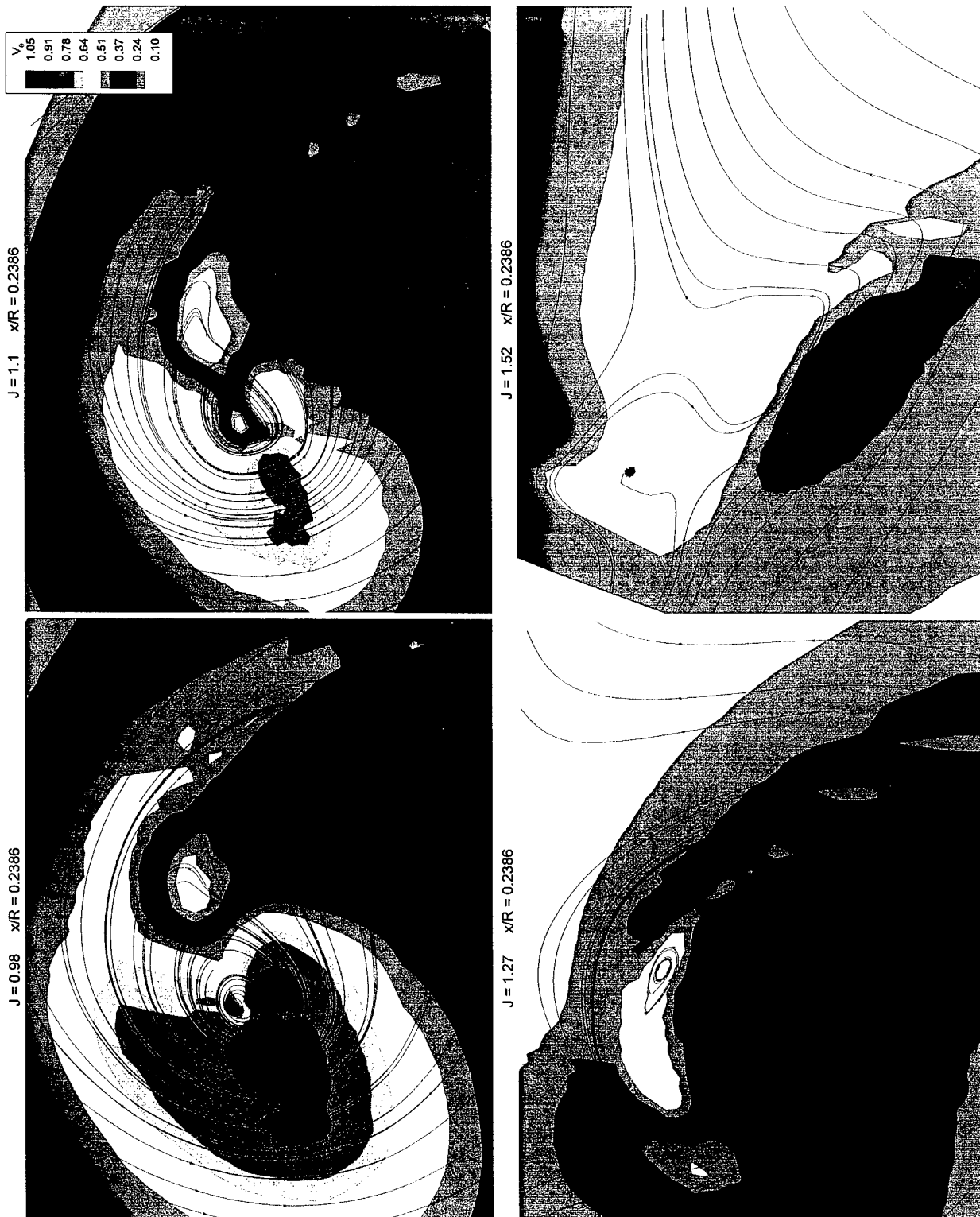


Fig. 27. Comparison of the tip-vortex region for differing advance coefficients, $x/R = 0.2386$.

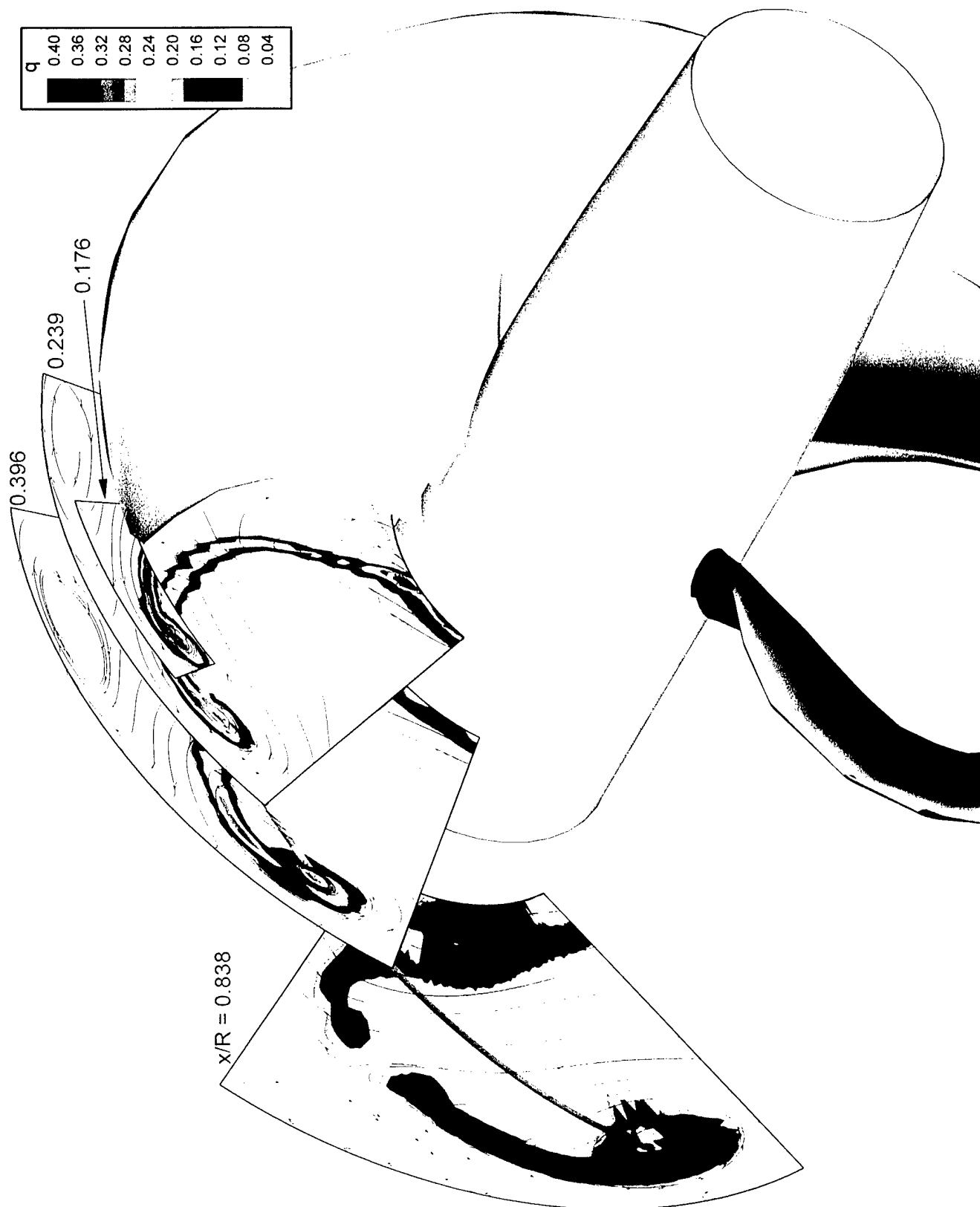


Fig. 28. Contours of q downstream of the propeller, $J = 1.10$.

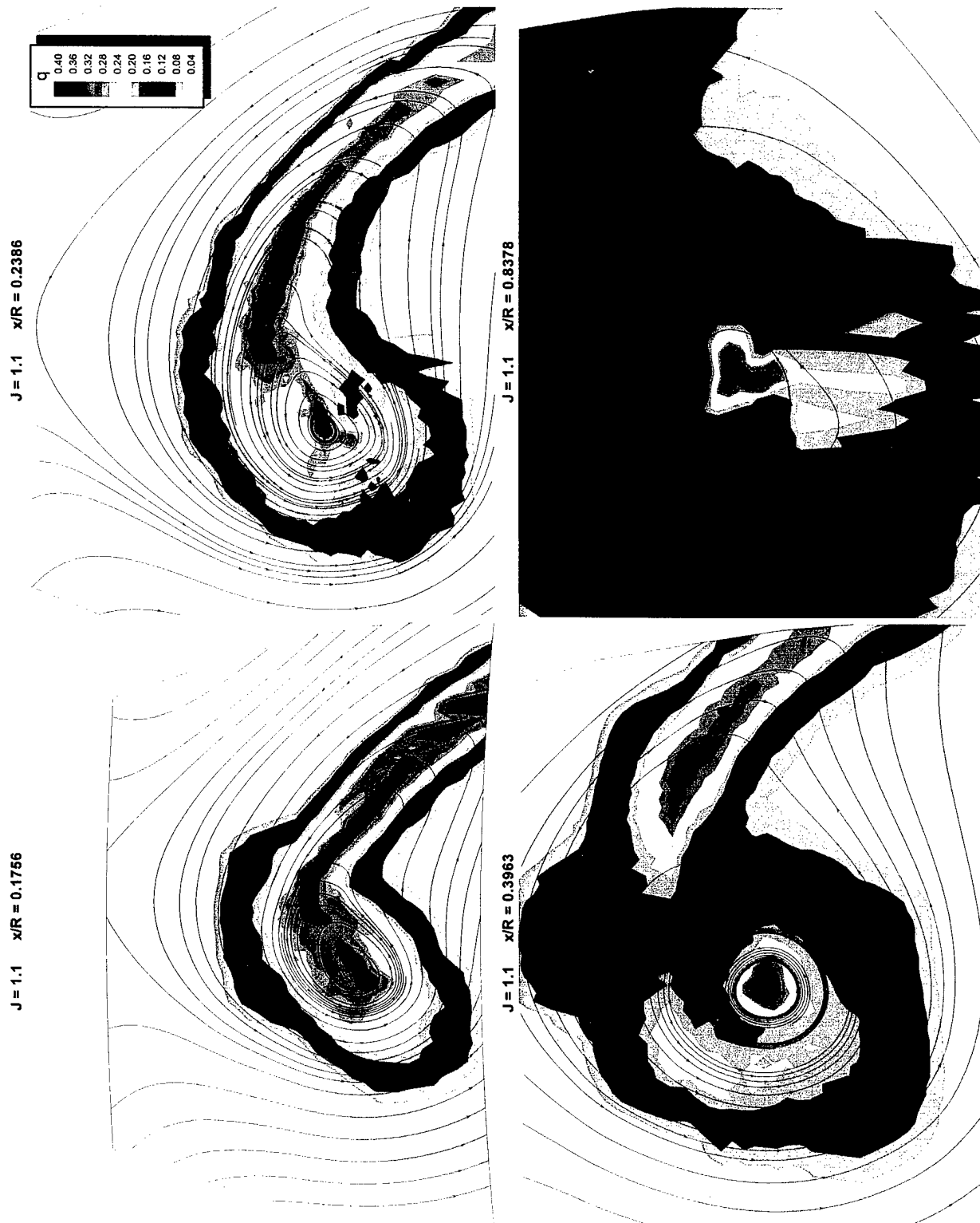


Fig. 29. Turbulence in the vortex, moving downstream, $J = 1.10$.

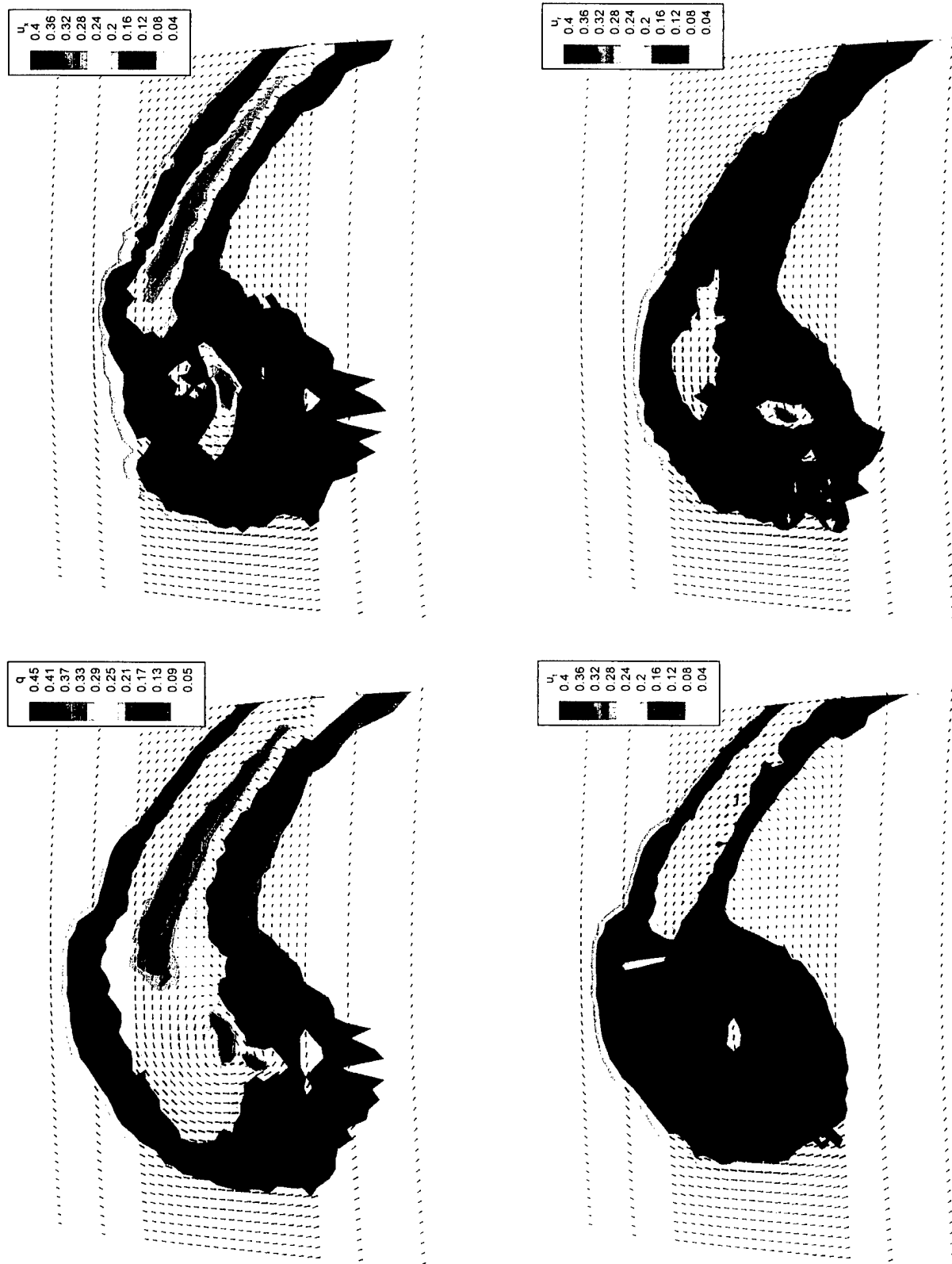


Fig. 30. Turbulence in the vortex, $x/R = 0.2386$, $J = 1.10$, hybrid LDV system.

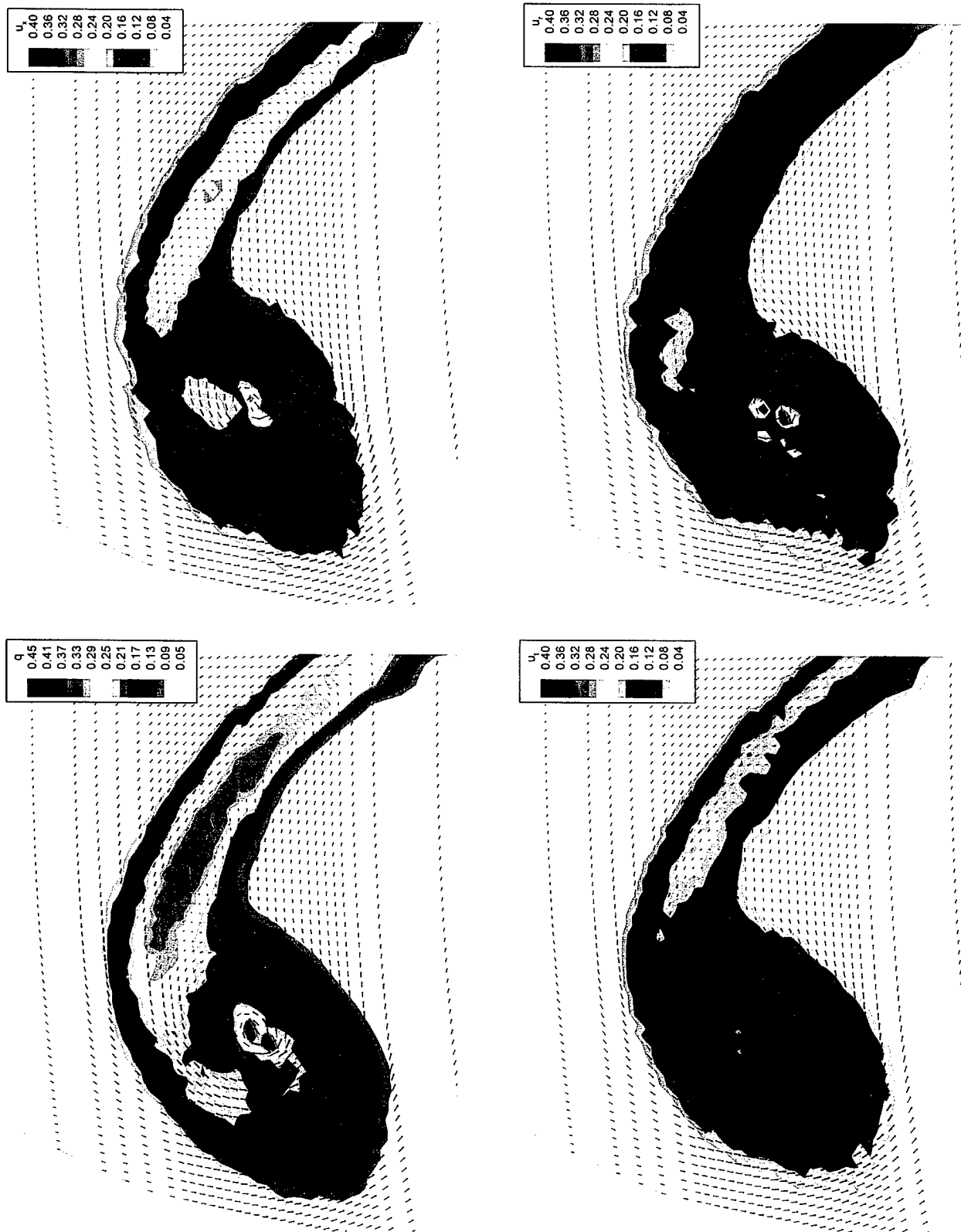


Fig. 31. Turbulence in the vortex, $x/R = 0.2386$, $J = 1.10$, fiber-optic LDV system.

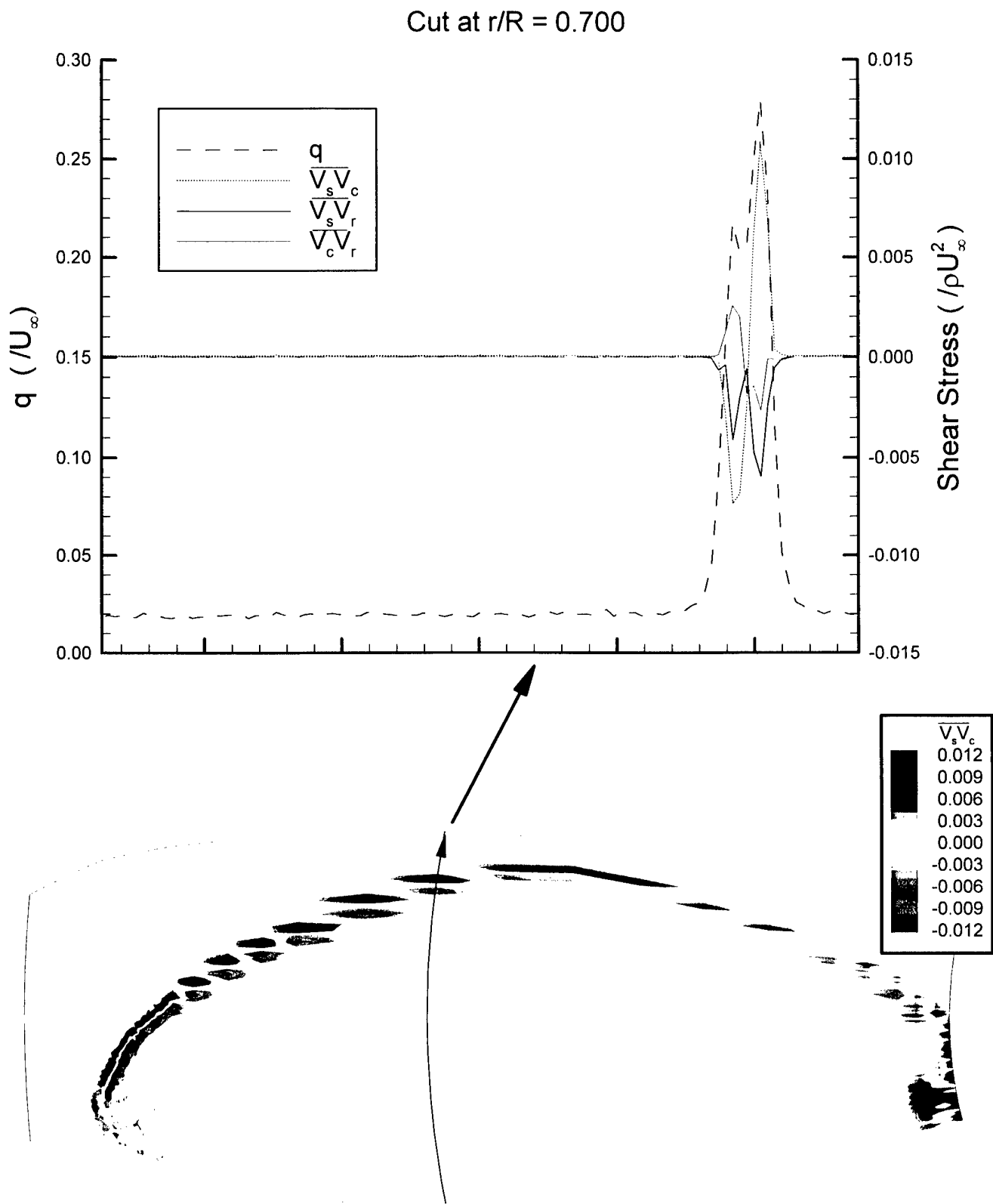


Fig. 32. Contours of $\overline{V_s V_c}$, with cut at $r/R = 0.700$, $x/R = 0.2386$, $J = 1.10$.

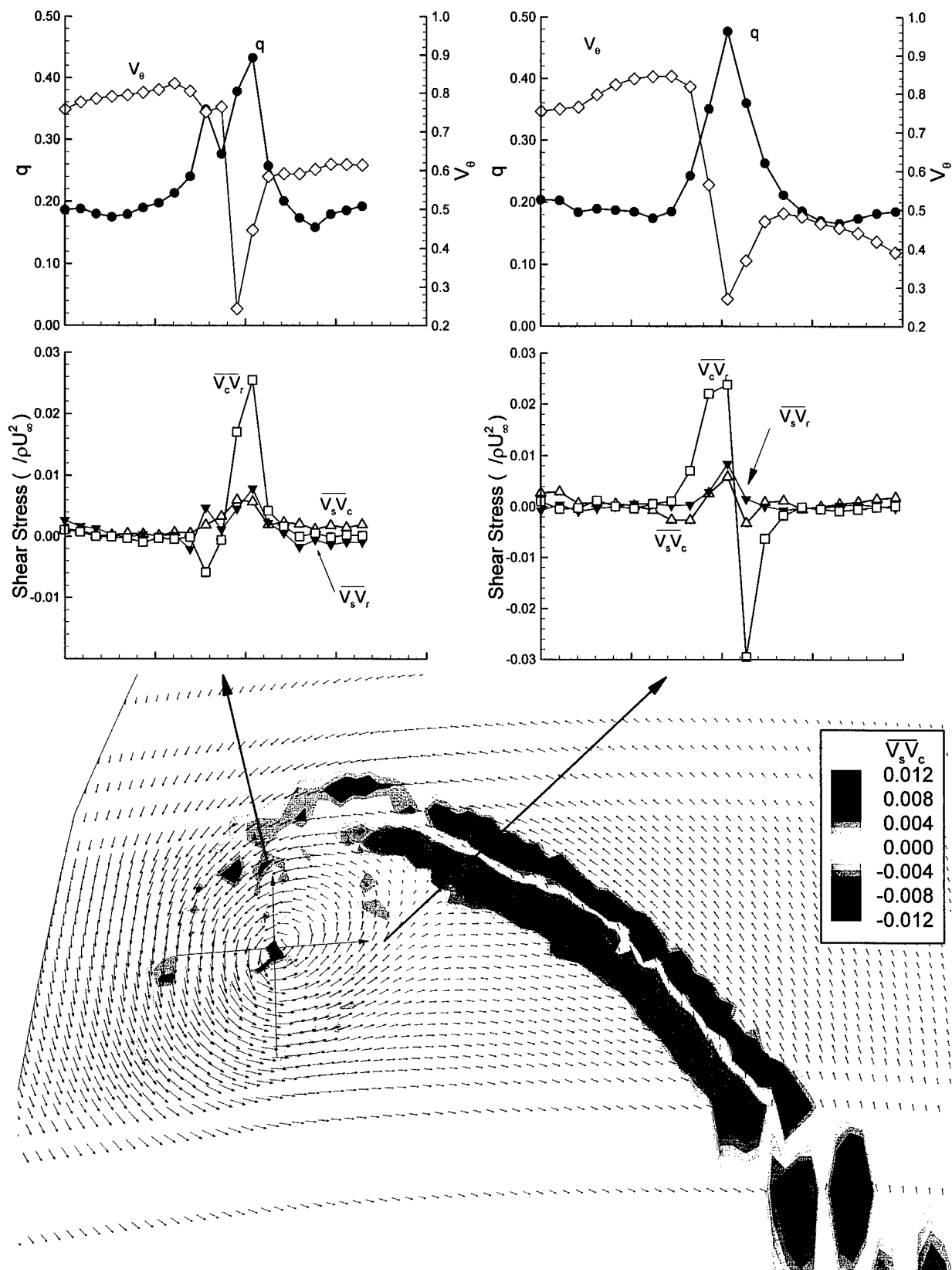


Fig. 33. Contours of $\overline{V_s V_c}$, with cuts through the vortex core, $x/R = 0.2386$, $J = 1.10$.

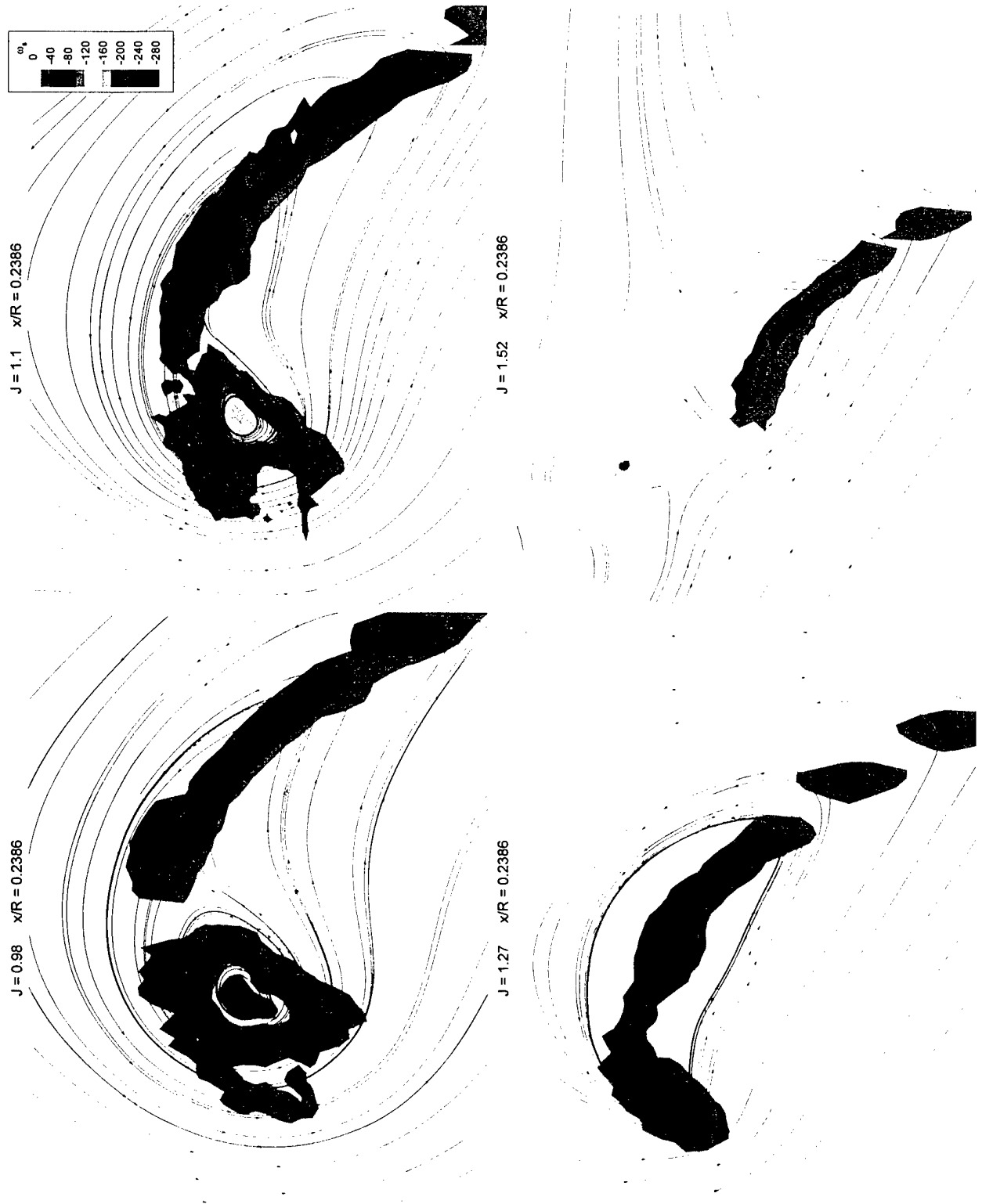


Fig. 34. Streamwise vorticity in the tip-vortex region, $x/R = 0.2386$.

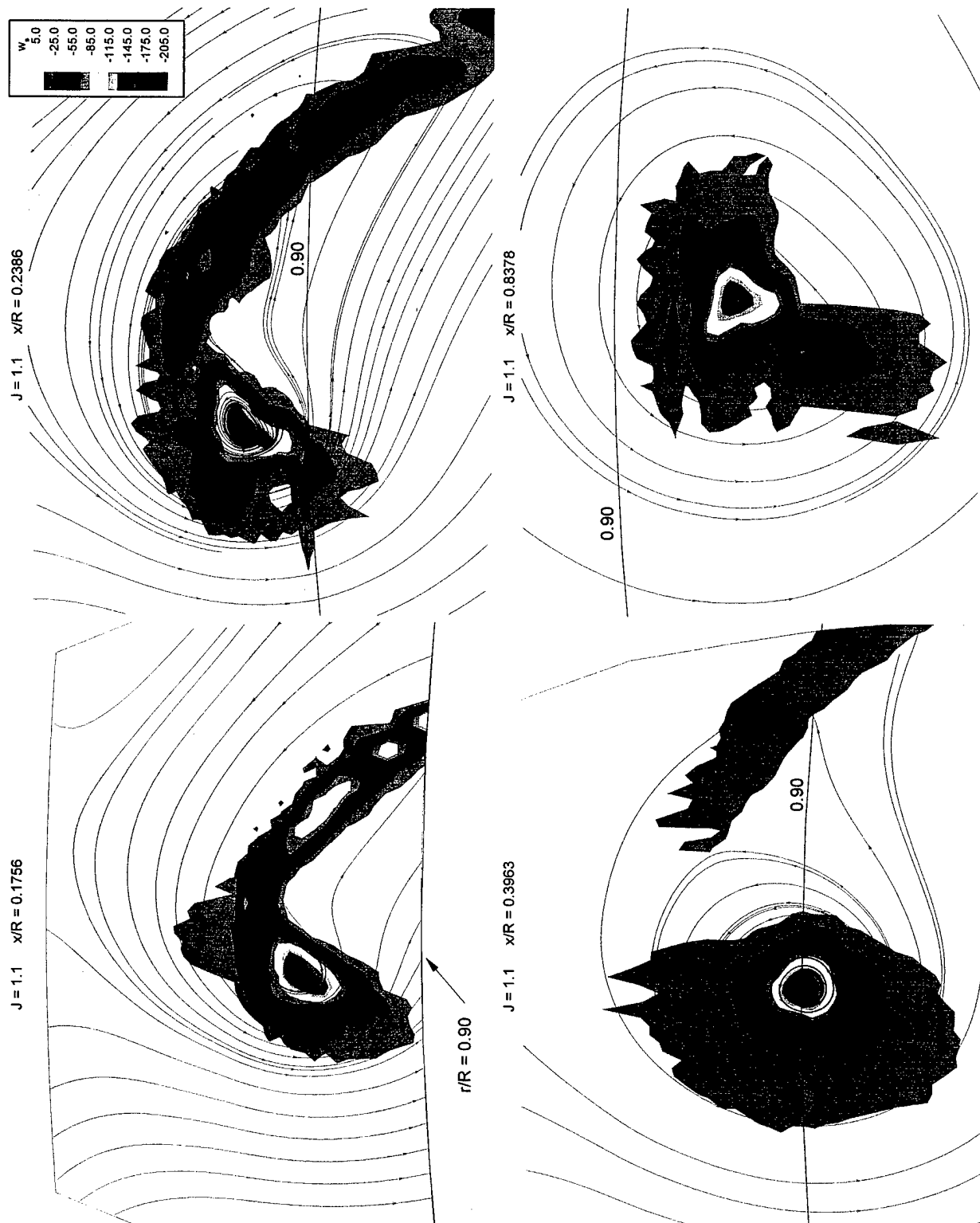


Fig. 35. Streamwise vorticity in the tip-vortex region, $J = 1.10$.

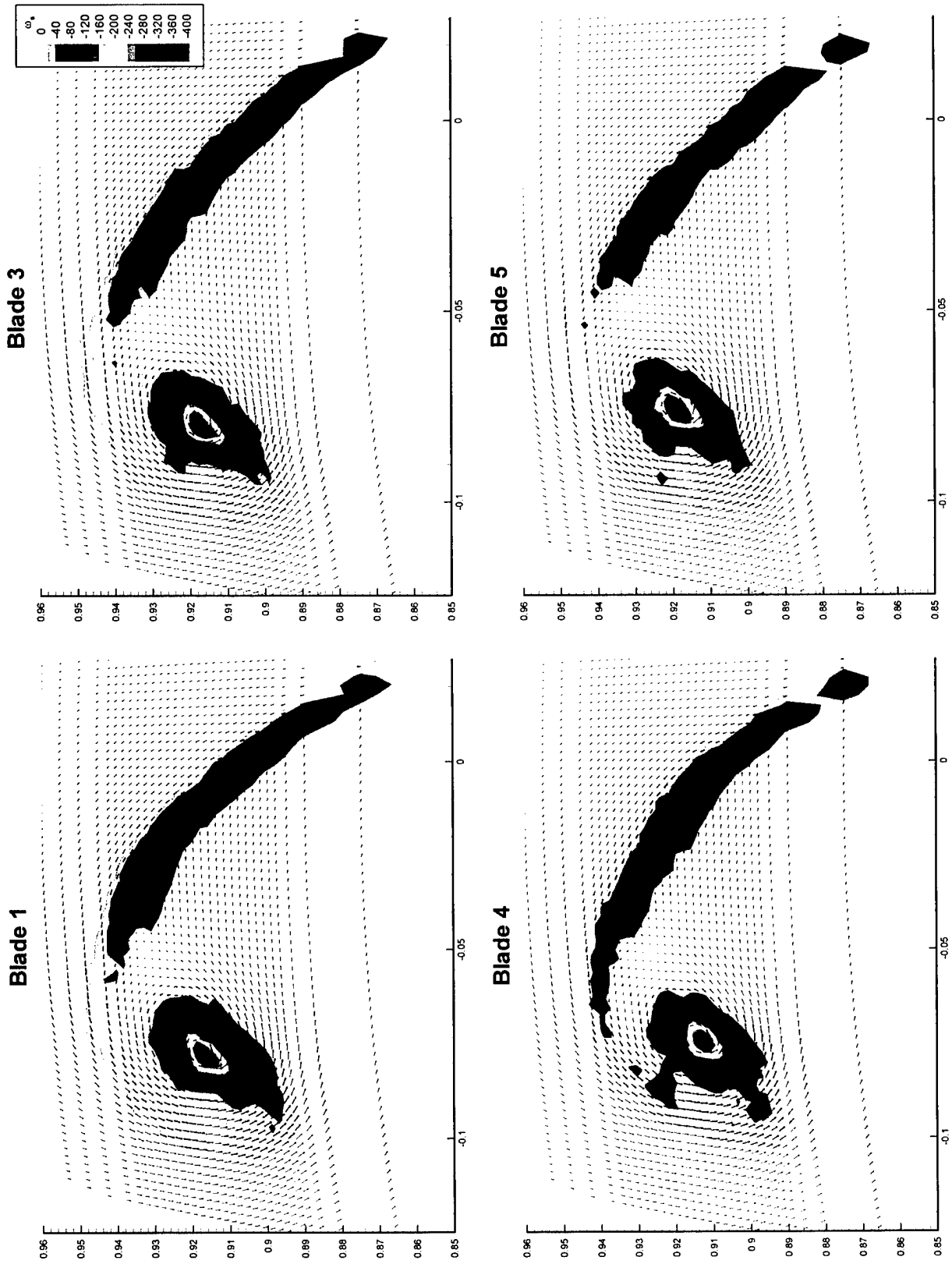


Fig. 36. Blade-to blade variation of ω_s , fiber-optic system, $x/R = 0.2386$, $J = 1.10$.



Fig. 37. Comparison of ω_s from hybrid and fiber-optic systems, $x/R = 0.2386$, $J = 1.10$.

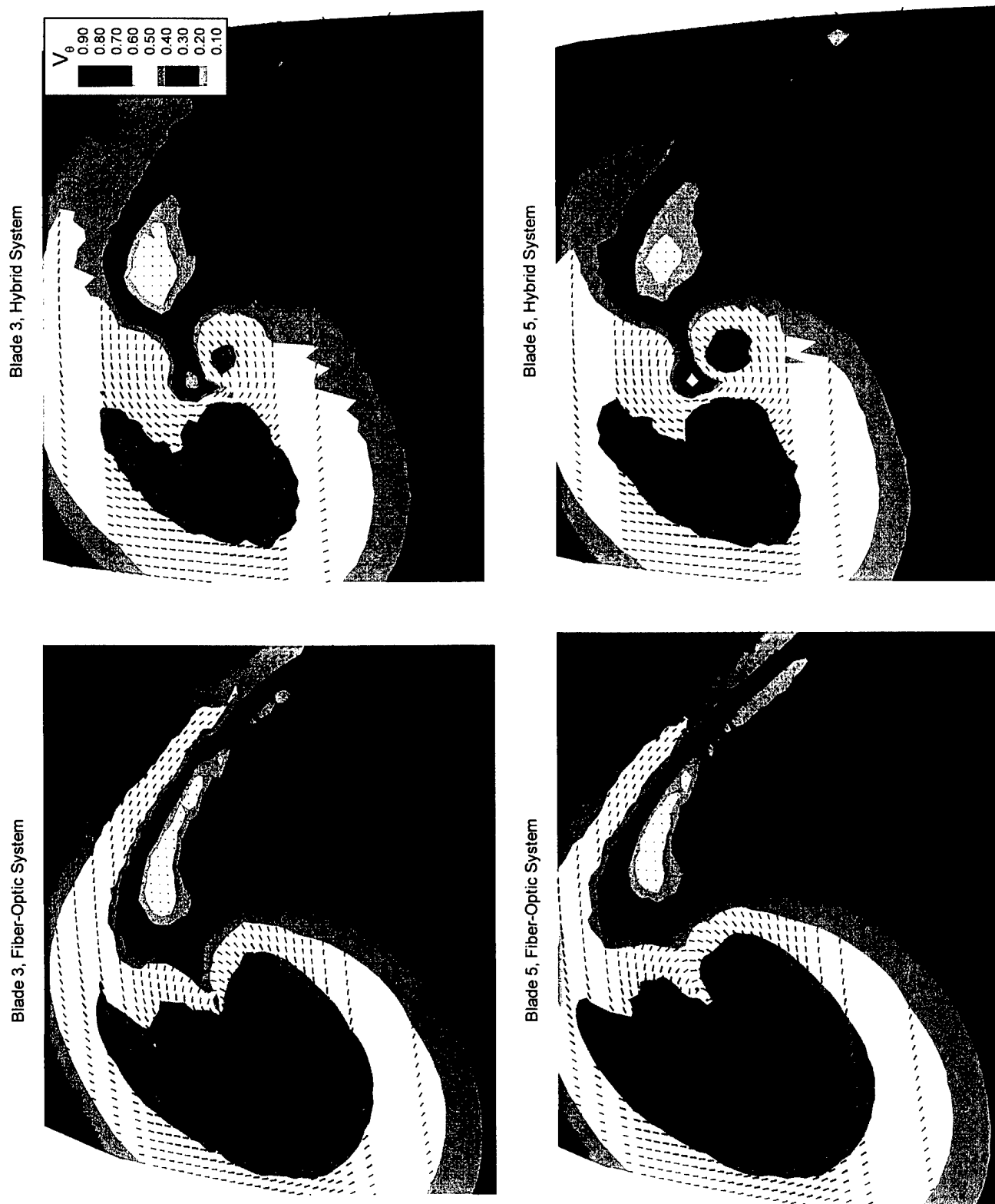


Fig. 38. Comparison of V_0 from hybrid and fiber-optic systems, $x/R = 0.2386$, $J = 1.10$.

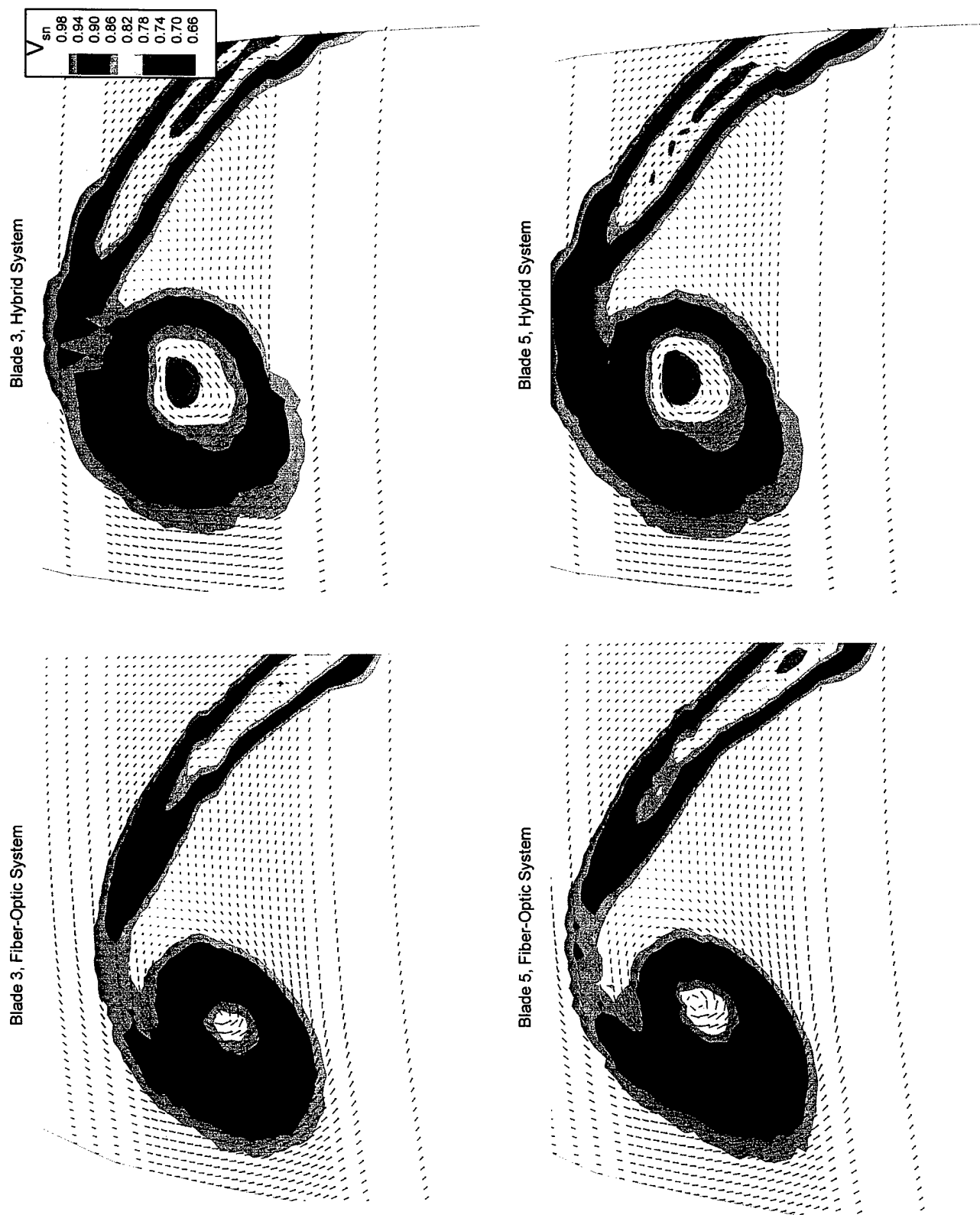


Fig. 39. Comparison of V_{sn} from hybrid and fiber-optic systems, $x/R = 0.2386$, $J = 1.10$.

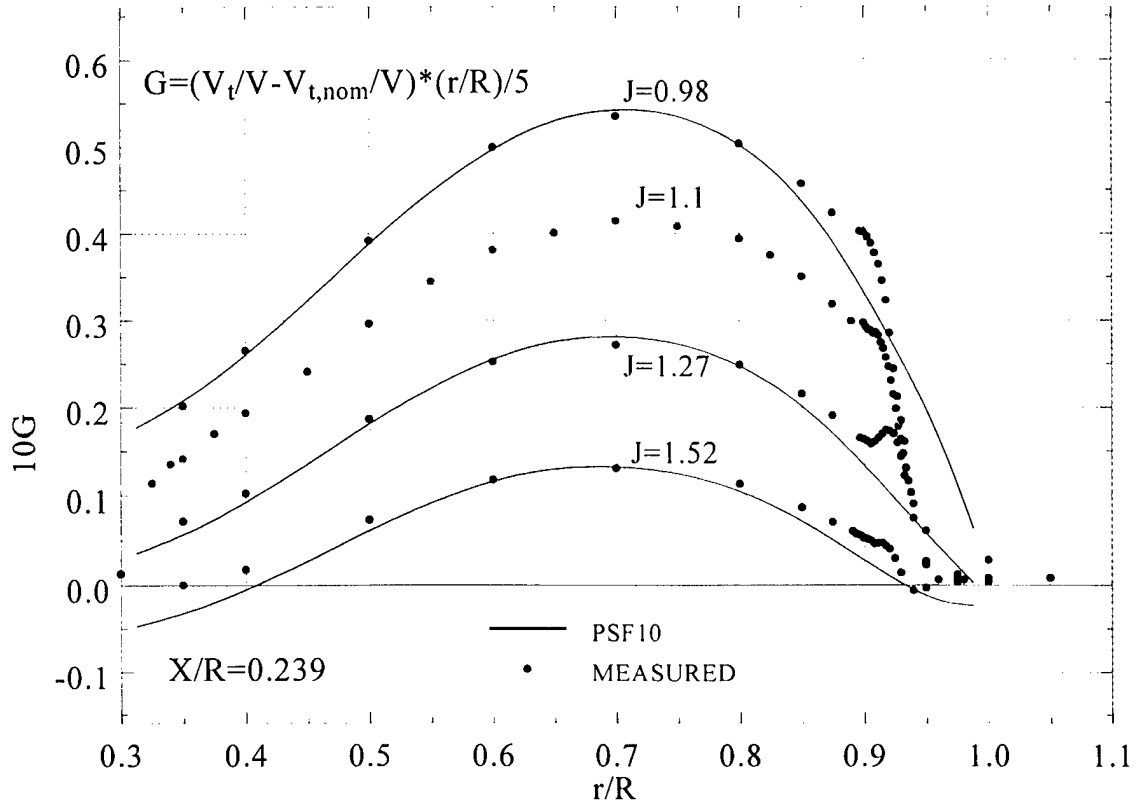


Fig. 40. Comparison of calculated and measured circulation distribution.

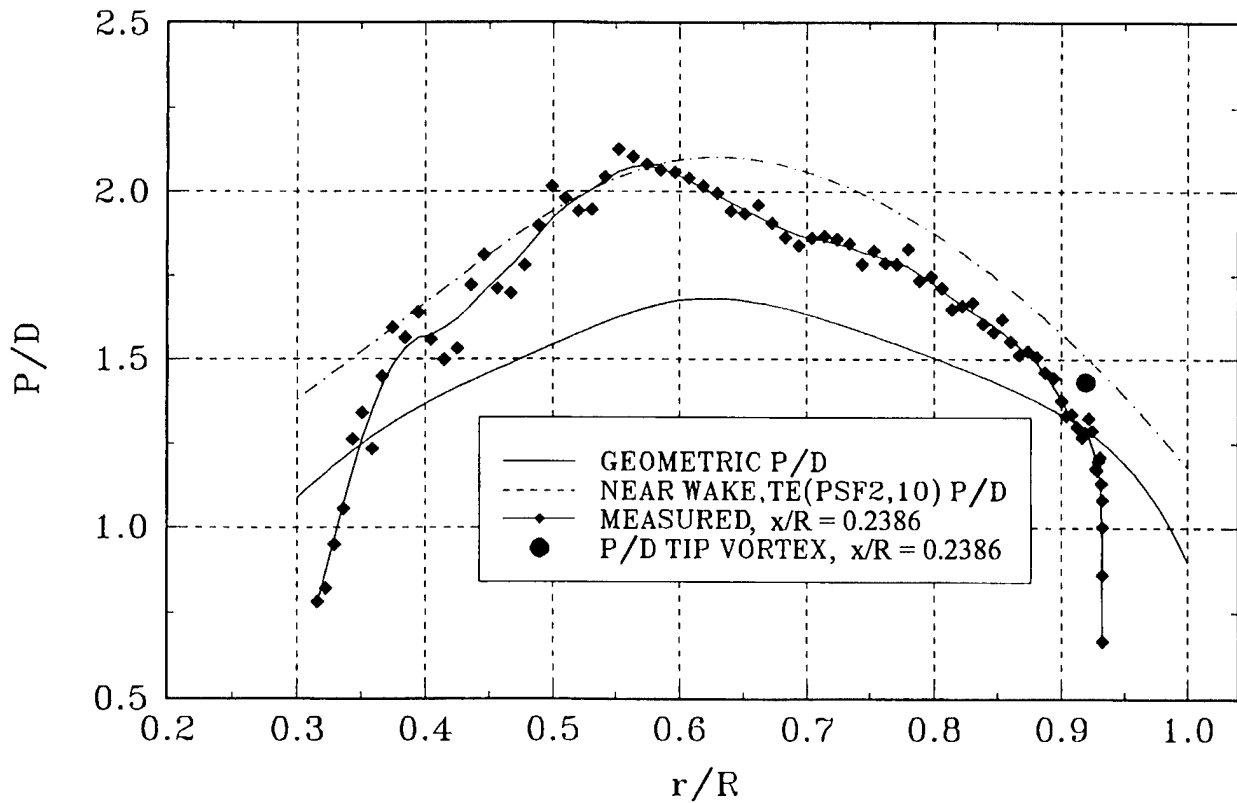


Fig. 41. Comparison of measured and calculated blade wake pitch.